RESEARCH ARTICLE

IL1-Induced JAK/STAT Signaling Is Antagonized by TGFβ to Shape CAF Heterogeneity in Pancreatic Ductal Adenocarcinoma

Giulia Biffi[1,2], Tobiloba E. Oni[1,2], Benjamin Spielman[1,2], Yuan Hao[1], Ela Elyada[1,2], Youngkyu Park[1,2], Jonathan Preall[1], and David A. Tuveson[1,2]

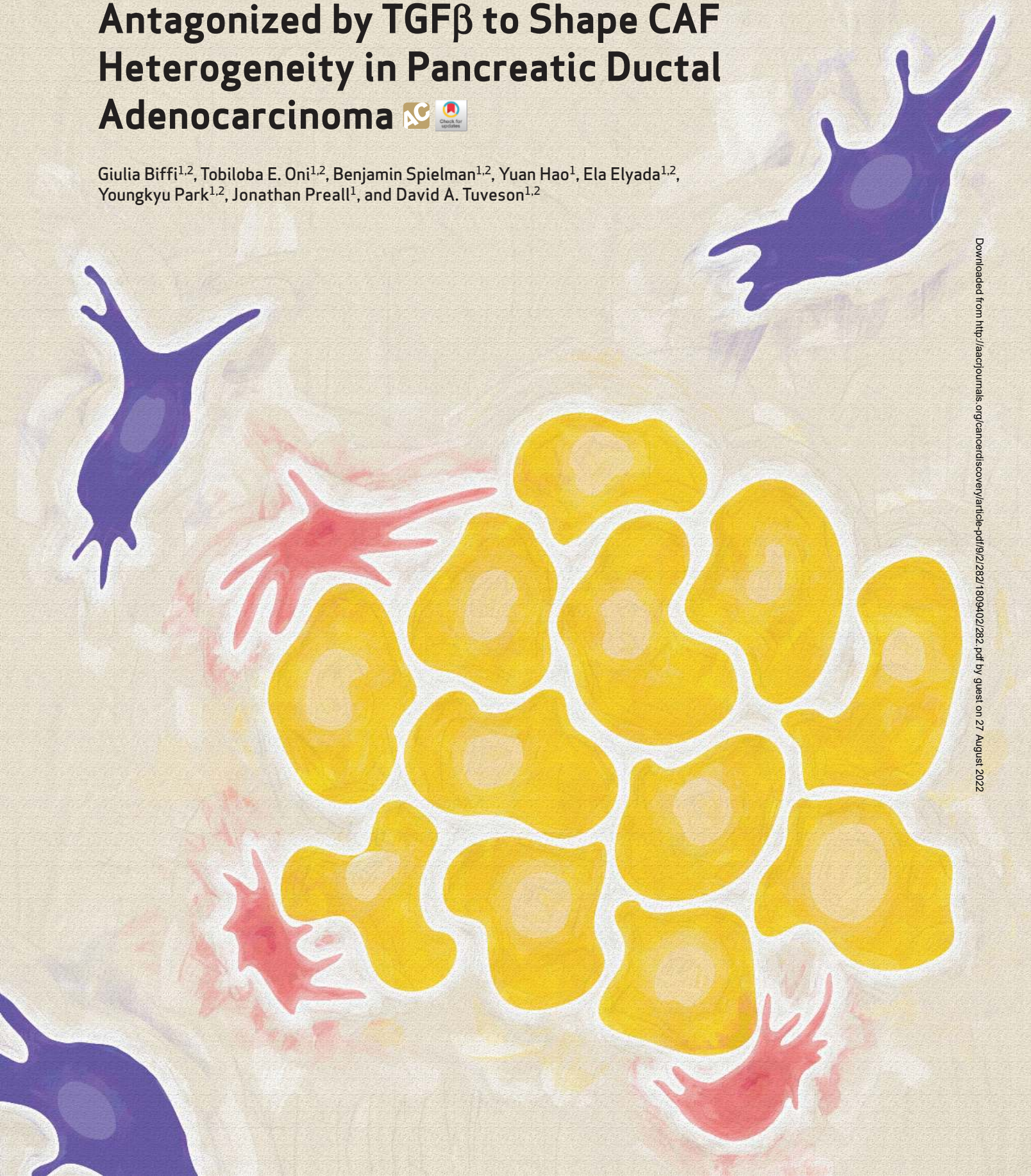

ABSTRACT Pancreatic ductal adenocarcinoma (PDAC) is poorly responsive to therapies and histologically contains a paucity of neoplastic cells embedded within a dense desmoplastic stroma. Within the stroma, cancer-associated fibroblasts (CAF) secrete tropic factors and extracellular matrix components, and have been implicated in PDAC progression and chemotherapy resistance. We recently identified two distinct CAF subtypes characterized by either myofibroblastic or inflammatory phenotypes; however, the mechanisms underlying their diversity and their roles in PDAC remain unknown. Here, we use organoid and mouse models to identify TGFβ and IL1 as tumor-secreted ligands that promote CAF heterogeneity. We show that IL1 induces LIF expression and downstream JAK/STAT activation to generate inflammatory CAFs and demonstrate that TGFβ antagonizes this process by downregulating IL1R1 expression and promoting differentiation into myofibroblasts. Our results provide a mechanism through which distinct fibroblast niches are established in the PDAC microenvironment and illuminate strategies to selectively target CAFs that support tumor growth.

SIGNIFICANCE: Understanding the mechanisms that determine CAF heterogeneity in PDAC is a prerequisite for the rational development of approaches that selectively target tumor-promoting CAFs. Here, we identify an IL1-induced signaling cascade that leads to JAK/STAT activation and promotes an inflammatory CAF state, suggesting multiple strategies to target these cells *in vivo*.

See related commentary by Ling and Chiao, p. 173.

INTRODUCTION

With an overall 5-year survival rate of less than 8%, pancreatic ductal adenocarcinoma (PDAC) is one of the cancers with the worst prognosis (1). Among the reasons for PDAC lethality, late diagnosis and resistance to chemotherapy play a central role. Factors that contribute to this resistance include the presence of a poorly vascularized, extensive stroma that acts as a barrier to drug delivery (2–5), and cytokines and growth factors secreted by nonneoplastic stromal cells that attenuate drug responses (6–10). Although numerous studies have focused on the genetic and epigenetic forces that drive PDAC progression, less is understood about the complex tumor microenvironment (TME).

Previous studies that targeted different stromal cell types or extracellular matrix components, such as hyaluronan, have highlighted the presence of both tumor-promoting and tumor-restraining components in the PDAC stroma. Among stromal cells, cancer-associated fibroblasts (CAF) have long been considered protumorigenic components of the PDAC TME, due to their involvement in desmoplasia, immunosuppression, and secretion of factors that promote cancer cell proliferation and survival (2, 4, 11, 12). However, in recent years, CAFs have been the focus of an active debate that has challenged this dogma. In mouse models of PDAC, targeting of the hedgehog (HH) pathway, which has been shown to stimulate CAF biology, by genetic deletion of the ligand sonic hedgehog or chronic chemical inhibition, led to more aggressive and poorly differentiated PDAC, with reduced stromal content and survival (13, 14). Furthermore, a clinical trial using inhibition of the HH pathway failed in advanced PDAC (15). These results suggest that at least a subset of CAFs plays a role in restricting, rather than promoting, tumor progression. Moreover, genetic ablation of cells expressing alpha smooth muscle actin (αSMA), a marker of myofibroblasts, led to similar results in a mouse model of PDAC (16), suggesting that perturbation of myofibroblastic components in the PDAC TME might promote tumor progression. Overall, these studies highlight the heterogeneity of PDAC stroma, prompting a more detailed examination of the role of the TME in PDAC progression, and calling for new therapeutic strategies that selectively target tumor-promoting CAF populations and spare tumor-restraining ones.

To better understand tumor–fibroblast interactions in PDAC, we recently established a system to coculture naïve pancreatic stellate cells (PSC), a precursor population of CAFs, with PDAC organoids derived from *Kras*$^{LSL\text{-}G12D/+}$; *Trp53*$^{LSL\text{-}R172H/+}$; *Pdx1*-Cre (KPC) mice, a genetically engineered mouse model that faithfully recapitulates human PDAC progression (17–19). Using this system, as well as *in vivo* mouse and human PDAC specimens, we identified two subtypes of CAFs: a population that expressed inflammatory markers such as IL6 and leukemia inhibitory factor (LIF) and was therefore named "inflammatory CAFs" (iCAF), and a population that expressed markers of myofibroblasts, such as αSMA, and was therefore named "myofibroblastic CAFs" (myCAF; ref. 19). Whereas myCAFs are found adjacent to tumor cells, iCAFs are located farther away within the dense stroma, suggesting that their different phenotypes might be related to their spatial distribution. Importantly, the presence of iCAF and myCAF populations in human PDAC

[1]Cold Spring Harbor Laboratory, Cold Spring Harbor, New York. [2]Lustgarten Foundation Pancreatic Cancer Research Laboratory, Cold Spring Harbor, New York.

Note: Supplementary data for this article are available at Cancer Discovery Online (http://cancerdiscovery.aacrjournals.org/).

Corresponding Author: David A. Tuveson, Cold Spring Harbor Laboratory, 1 Bungtown Road, Cold Spring Harbor, New York, NY 11724. Phone: 516-367-5246; Fax: 516-367-8353; E-mail: dtuveson@cshl.edu

doi: 10.1158/2159-8290.CD-18-0710

in vivo has been recently confirmed (20). However, the signals that drive the formation of these distinct populations are not known. To better understand the mechanisms that promote the formation of these two CAF populations in PDAC, we focused on the identification of tumor-secreted ligands and signaling pathways responsible for their respective phenotypes.

RESULTS

Active NF-κB Signaling Is Associated with the iCAF Phenotype

We first sought to define signaling pathways that are upregulated in iCAFs compared with myCAFs and quiescent PSCs. Targeting this CAF population might be therapeutically beneficial, as many of the factors secreted by iCAFs, such as IL6, G-CSF, CXCL1, and LIF, have been shown to play a role in tumor progression (21–24). We hypothesized that NF-κB signaling might play a role in iCAF formation, because it has been previously identified as a pathway responsible for the induction of an inflammatory profile in CAFs (25, 26).

The role of the NF-κB pathway and of its activating ligands IL1 and TNFα in PDAC progression have been mostly studied in the context of the epithelial compartment (27–31). However, some studies have reported a role of tumor-secreted IL1 and TNFα in remodeling PDAC stroma (32–34). In particular, IL1α has been shown to induce the expression of IL6 and CXCL8 in PDAC CAFs *in vitro* (32). To determine whether IL1 and TNFα signaling can be activated in PDAC CAFs *in vivo*, we sorted neoplastic epithelial cells and CAFs from tumors isolated from KPC mice. Epithelial cell adhesion molecule (EPCAM) and PDGFRα/podoplanin (PDPN) expression were used to sort epithelial cells and CAFs, respectively (Supplementary Fig. S1A). qPCR analysis of the sorted populations showed that *Il1a* and *Tnf* were more highly expressed in epithelial cancer cells relative to CAFs, whereas the corresponding receptors that trigger NF-κB activation (*Il1r1* and *Tnfrsf1a*) were predominantly expressed in CAFs (Fig. 1A). Consistent with this observation, flow-cytometric analysis of CAFs and epithelial cells isolated from KPC tumors identified higher levels of IL1R1 protein in CAFs compared with epithelial cancer cells (Fig. 1B; Supplementary Fig. S1B). As a complementary approach, single-cell RNA-sequencing analysis of KPC tumors confirmed higher expression of the ligands activating the NF-κB pathway in epithelial cells and higher expression of their receptors in CAFs (Fig. 1C; Supplementary Fig. S1C). Altogether, these results demonstrate that CAFs are poised to respond to the ligands that activate the NF-κB pathway.

Although IL1β was not detectable *in vitro* (data not shown), IL1α and TNFα were detectable by ELISA in conditioned media from tumor and metastatic organoids as well as monolayer KPC cell lines, but not in conditioned media from fibroblasts. This agrees with the observation that fibroblasts are not capable of stimulating iCAF formation (ref. 19; Fig. 1D; Supplementary Fig. S1D).

To model iCAF, myCAF, and quiescent fibroblast states, we used distinct culture conditions (19). PSCs embedded in Matrigel and cultured in control media (5% FBS/DMEM) maintain a quiescent phenotype. In contrast, PSCs embedded in Matrigel and cultured in a transwell system with tumor organoids or exposed to tumor organoid–conditioned media acquire an inflammatory phenotype characteristic of iCAFs. Finally, PSCs cultured in monolayer acquire the myofibroblastic features typical of myCAFs (Supplementary Fig. S1E).

To verify that the *in vitro* culture systems used to model iCAFs and myCAFs closely resemble the *in vivo* setting, we analyzed the single-cell RNA-sequencing data set of KPC tumors. Confirming our previous findings (19), single-cell RNA-sequencing analysis of KPC tumors revealed *in vivo* presence of both iCAF and myCAF populations (Supplementary Fig. S1F). Similar to what observed *in vitro* (19), the iCAFs and myCAFs identified *in vivo* segregated into two distinct clusters (Supplementary Fig. S1G). We then compared the gene-expression profiles of myCAFs and iCAFs identified *in vivo* with the gene-expression profiles of myCAFs and iCAFs cultured *in vitro*, as previously reported by our laboratory (19). Venn diagrams of genes upregulated in iCAFs or myCAFs showed significant overlap between the *in vivo* and *in vitro* data sets (Supplementary Fig. S1H), supporting the *in vivo* relevance of our *in vitro* model. To further strengthen this, gene set enrichment analysis (GSEA) of iCAFs and myCAFs identified *in vivo* revealed several differentially expressed pathways that were previously identified by our laboratory using the *in vitro* system (19). For instance, the JAK/STAT pathway was upregulated in iCAFs compared with myCAFs, whereas collagen formation and TGFβ signaling pathways were downregulated in iCAFs compared with myCAFs (Supplementary Fig. S1I).

Having established the reliability of our *in vitro* system, we first investigated whether the NF-κB pathway has a role in iCAF formation. Using the *in vitro* culture conditions described (Supplementary Fig. S1E), we prepared nuclear

Figure 1. Active NF-κB signaling is associated with the iCAF phenotype. **A,** qPCR analysis of *Il1a, Il1b, Tnf, Il1r1, Tnfrsf1a*, and epithelial (*Epcam* and *Cdh1*) and fibroblast (*Pdgfra, Pdpn,* and *Col1a1*) markers in EPCAM$^+$ (epithelial cells) relative to PDPN$^+$ (CAFs) cells sorted from KPC tumors. Results show mean ± SEM of 6 biological replicates. *, $P < 0.05$; **, $P < 0.01$; ***, $P < 0.001$, paired Student *t* test. **B,** Representative flow-cytometric analysis of IL1R1 in EPCAM$^+$ (epithelial cells) and PDPN$^+$ (CAFs) cells in KPC tumors ($n = 3$). Percentages shown were calculated from the parental gate. **C,** Violin plots showing single-cell RNA-sequencing analysis of *Il1a, Il1b, Il1r1, Epcam,* and *Col1a1* of a representative KPC tumor ($n = 2$) in CAFs (orange) and epithelial cells (green). **D,** ELISA of IL1α from media of mouse monolayer KPC cells ($n = 2$), tumor (T; $n = 8$) and metastatic (M; $n = 8$) organoids, and controls (Matrigel, monolayer 3T3, and monolayer PSCs) that do not induce the iCAF phenotype ($n = 2$ for each control). Results show mean ± SEM. **E,** Western blot analysis of the nuclear factor NF-κB p65 subunit following nuclear fractionation of quiescent PSCs (qP; PSCs cultured in Matrigel with control media, i.e., 5% FBS DMEM, for 4 days), iCAFs (iC; PSCs cultured in Matrigel with tumor organoid–conditioned media for 4 days) and myCAFs (myC; PSCs cultured in monolayer with 5% FBS DMEM). Loading controls, HSP90α (cytoplasmic fractions), and H3 (nuclear fractions). The same amount of protein lysate was loaded in each lane. **F,** Western blot analysis of total and phosphorylated p65 (p-p65) and of total IκBα in PSCs cultured in Matrigel in control media or tumor organoid–conditioned media (CM) in the presence or absence of 30 μmol/L IKKβ inhibitor (IKKβi) ML102B for 30 minutes. Loading control, ACTIN. **G,** qPCR analysis of iCAF markers (*Il1a, Il6, Lif, Cxcl1,* and *Csf3*) in PSCs cultured in Matrigel with control media or tumor organoid–conditioned media for 1 hour in the presence or absence of 30 μmol/L ML102B. Results show mean ± SEM of 3 biological replicates. *, $P < 0.05$; **, $P < 0.01$, paired Student *t* test.

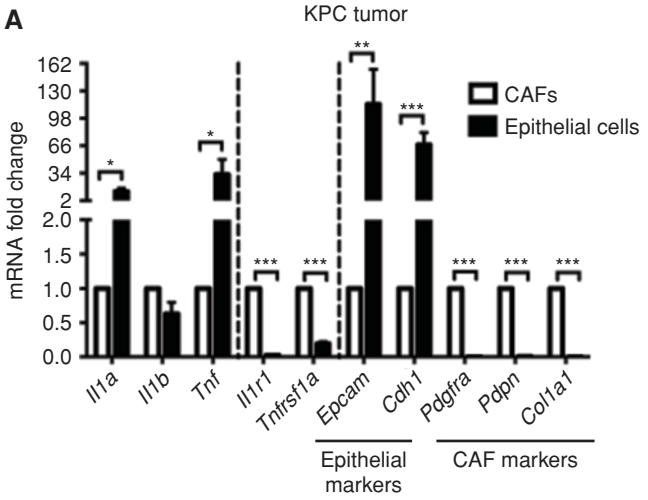

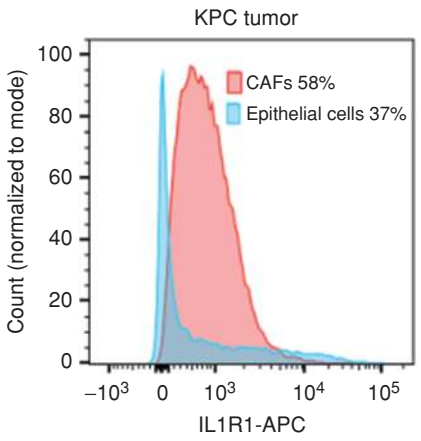

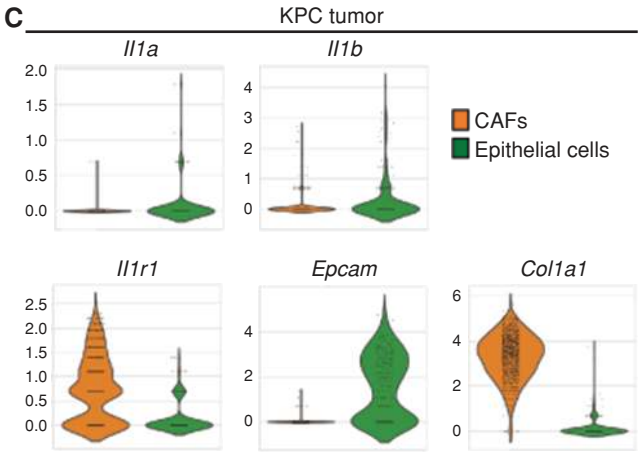

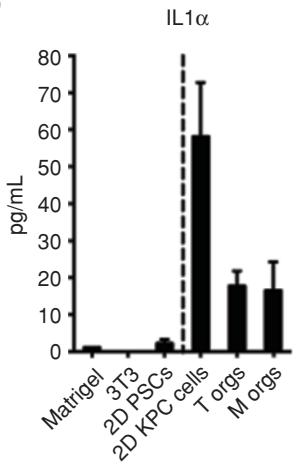

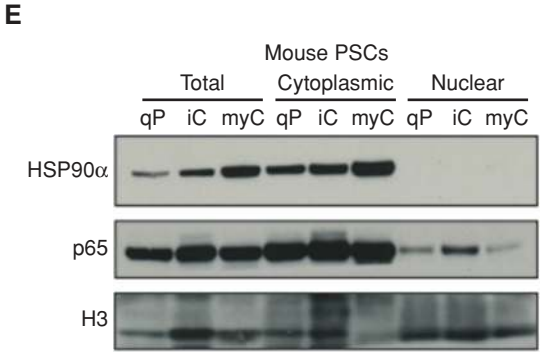

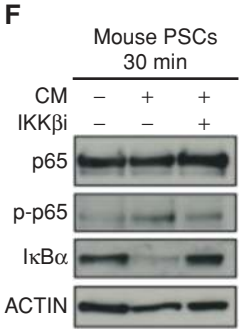

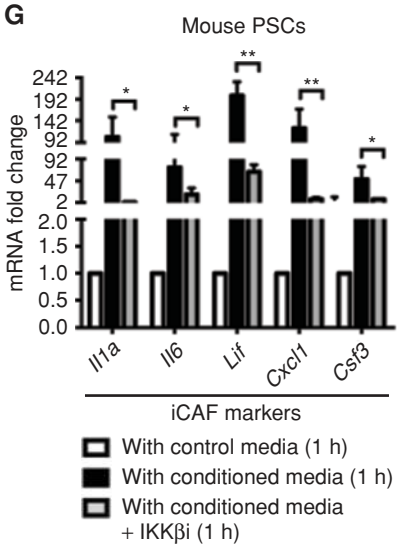

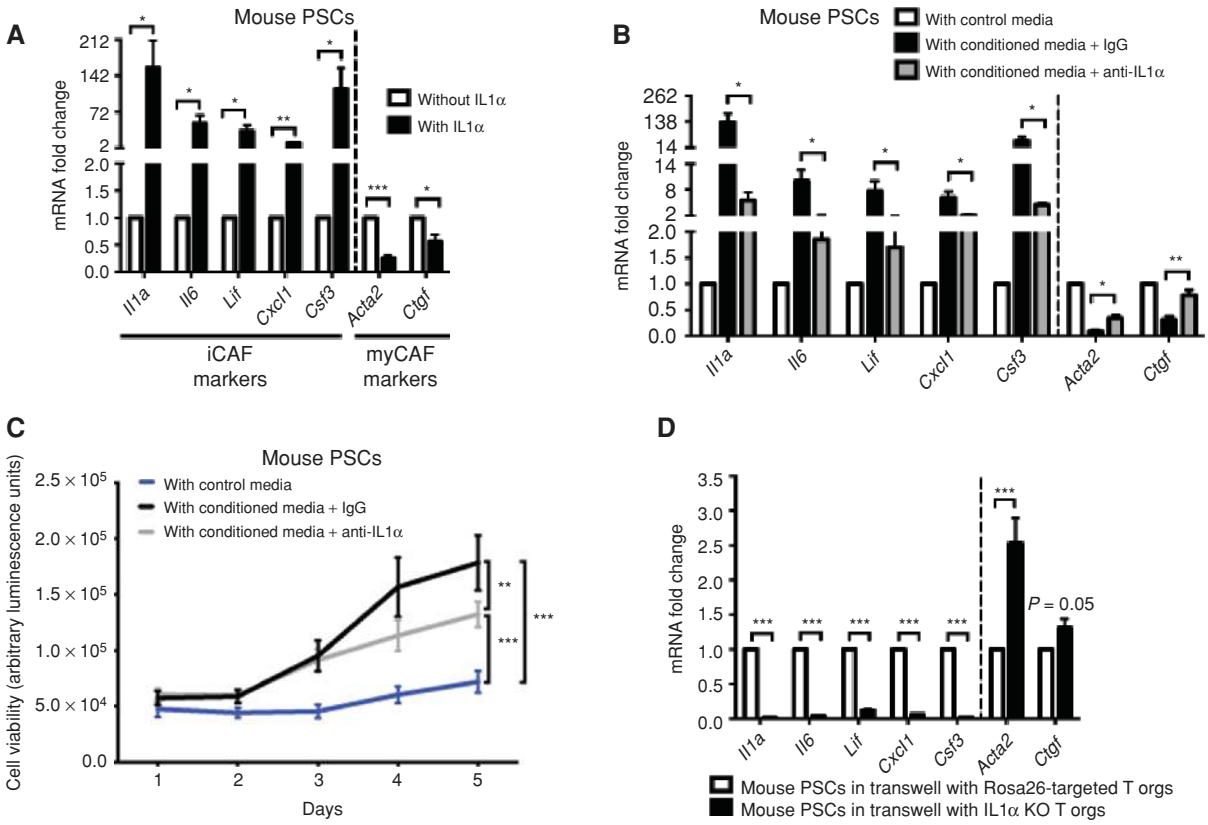

Figure 2. IL1 signaling is the main pathway responsible for the induction of an inflammatory phenotype in CAFs. **A,** qPCR analysis of iCAF (*Il1a, Il6, Lif, Cxcl1,* and *Csf3*) and myCAF (*Acta2* and *Ctgf*) markers in PSCs cultured in Matrigel in control media in the presence or absence of 1 ng/mL mouse IL1α for 4 days. Results show mean ± SEM of 2 biological replicates. *, $P < 0.05$; **, $P < 0.01$; ***, $P < 0.001$, paired Student *t* test. **B,** qPCR analysis of *Il1a, Il6, Lif, Cxcl1, Csf3, Acta2,* and *Ctgf* in PSCs cultured in Matrigel with control media or tumor organoid–conditioned media in the presence of a neutralizing antibody targeting IL1α or an IgG control for 4 days. Results show mean ± SEM of 6 biological replicates. *, $P < 0.05$; **, $P < 0.01$, paired Student *t* test. **C,** Proliferation curves of PSCs cultured in Matrigel with control media or tumor organoid–conditioned media in the presence of a neutralizing antibody targeting IL1α or an IgG control. Results show mean ± SEM of 3 biological replicates. **, $P < 0.01$; ***, $P < 0.001$, unpaired Student *t* test calculated for the last time point. **D,** qPCR analysis of *Il1a, Il6, Lif, Cxcl1, Csf3, Acta2,* and *Ctgf* in PSCs cultured in Matrigel in transwell with Rosa26-targeted controls or IL1α knockout (KO) tumor organoids (T orgs) for 4 days. Results show mean ± SEM of 9 and 11 biological replicates, respectively. ***, $P < 0.001$, paired Student *t* test. (*continued on following page*)

protein extracts from quiescent PSCs, iCAFs, and myCAFs and evaluated activation of the NF-κB pathway. Fractionation experiments revealed that nuclear levels of the NF-κB p65 subunit were more elevated in iCAFs compared with quiescent PSCs and myCAFs (Fig. 1E). Moreover, activation of p65 occurred rapidly in PSCs cultured in Matrigel upon addition of tumor organoid–conditioned media, as shown by increased levels of phosphorylated p65, parallel to phosphorylation of the NF-κB inhibitor IκBα (pIκBα), which is followed by its rapid degradation (Supplementary Fig. S1J), suggesting a role of the NF-κB pathway in iCAF formation. Treatment with ML102B, which targets IKKβ (35), impaired activation of the pathway, as shown by inhibition of p65 phosphorylation and stabilization of total IκBα (Fig. 1F). To confirm that NF-κB promotes iCAF formation, we thus determined the effects of NF-κB pathway inhibition on the expression of iCAF markers, such as *Il1a, Il6, Lif, Cxcl1,* and *Csf3* (encoding for G-CSF). Inhibition of NF-κB signaling impaired the ability of tumor organoid–conditioned media to induce iCAF marker genes in PSCs, supporting the premise that NF-κB signaling is required for the formation of iCAFs (Fig. 1G).

IL1 Signaling Is the Main Pathway Responsible for the Induction of an Inflammatory Phenotype in CAFs

To evaluate whether ligands that activate the NF-κB pathway induce the iCAF phenotype in quiescent PSCs, we cultured mouse and human PSCs in Matrigel in the presence or absence of IL1α. In response to IL1α, both mouse and human PSCs increased expression of multiple inflammatory cytokines and chemokines, such as *Il1a, Il6, Lif, Cxcl1,* and *Csf3* (Fig. 2A; Supplementary Fig. S2A and S2B). In parallel, IL1α treatment led to a decreased expression of myofibroblastic genes, such as the TGFβ target gene *Ctgf* and the αSMA gene *Acta2*, suggesting that IL1α promotes the iCAF phenotype (ref. 19; Fig. 2A; Supplementary Fig. S2A and S2B). Similar to IL1α, IL1β and TNFα were also sufficient to induce iCAF marker genes and downregulate myofibroblastic genes in PSCs (Supplementary Fig. S2C).

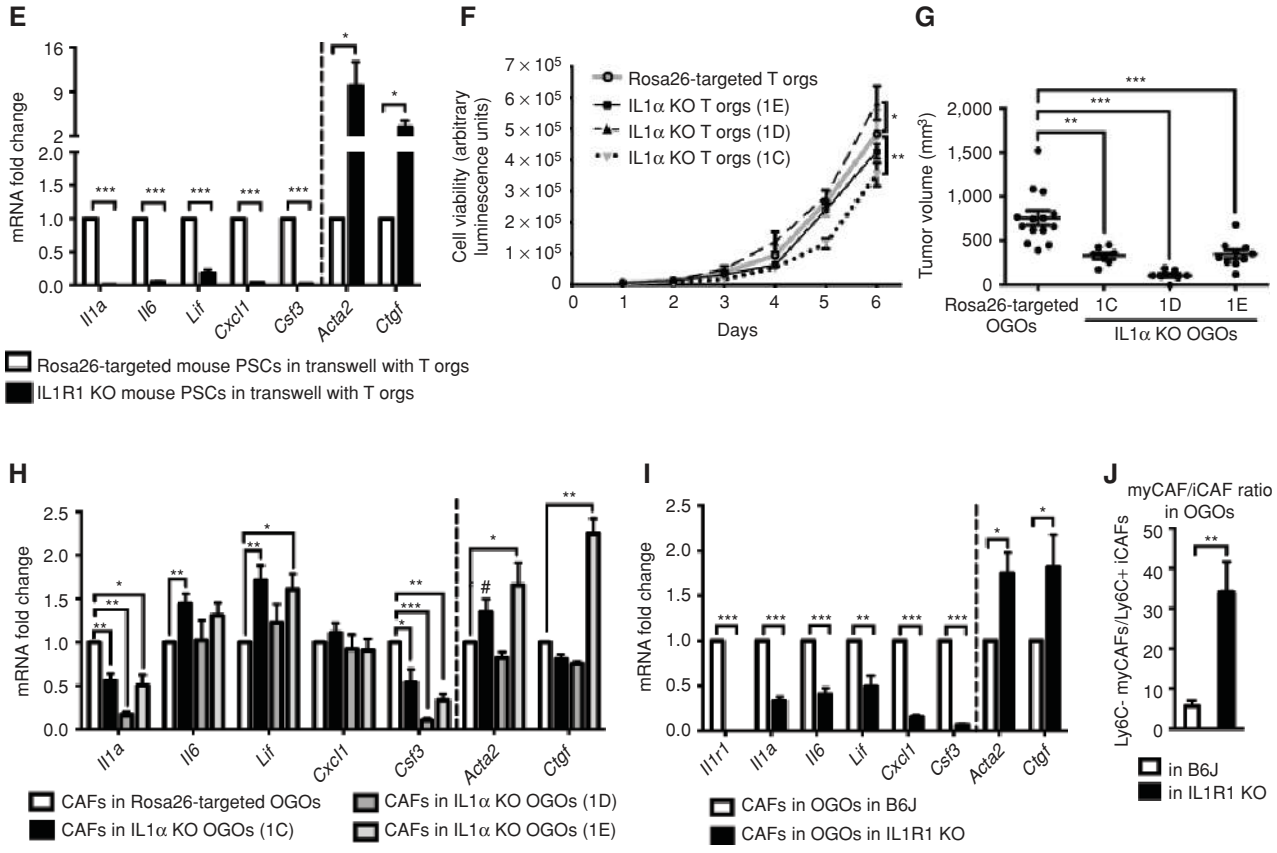

Figure 2. ***(Continued)*** **E,** qPCR analysis of *Il1a, Il6, Lif, Cxcl1, Csf3, Acta2,* and *Ctgf* in Rosa26-targeted controls and IL1R1 knockout PSCs cultured in Matrigel in transwell with tumor organoids for 4 days. Results show mean ± SEM of 7 biological replicates. *, $P < 0.05$; ***, $P < 0.001$, paired Student *t* test. **F,** Proliferation curves of Rosa26-targeted controls and IL1α knockout tumor organoids. Results show mean ± SD (standard deviation) of 5 technical replicates. *, $P < 0.05$; **, $P < 0.01$, unpaired Student *t* test calculated for the last time point. **G,** Tumor volume analysis based on ultrasound measurements of orthotopically grafted organoids (OGO) following ~3 weeks from transplantation of Rosa26-targeted controls and IL1α knockout tumor organoids in nu/nu mice. Results show mean ± SEM of 14 (control OGOs), 7 (1C or 1D OGOs), and 8 (1E OGOs) biological replicates. **, $P < 0.01$; ***, $P < 0.001$, unpaired Student *t* test. **H,** qPCR analysis of *Il1a, Il6, Lif, Cxcl1, Csf3, Acta2,* and *Ctgf* in CAFs sorted from OGOs derived from transplantation of Rosa26-targeted controls and IL1α knockout tumor organoids in nu/nu mice. Results show mean ± SEM of 12 (control OGOs), 7 (1C and 1E OGOs), and 5 (1D OGOs) biological replicates. *, $P < 0.05$; **, $P < 0.01$; ***, $P < 0.001$; #, $P = 0.06$, paired Student *t* test. **I,** qPCR analysis of *Il1a, Il6, Lif, Cxcl1, Csf3, Acta2, Ctgf,* and *Il1r1* in CAFs sorted from tumors derived by orthotopic transplantation of 3 tumor organoid lines in IL1R1 knockout or B6J controls. Results show mean ± SEM of 9 biological replicates. *, $P < 0.05$; **, $P < 0.01$; ***, $P < 0.001$, paired Student *t* test. **J,** Quantification of Ly6C- myCAF/Ly6C+ iCAF ratio in tumors derived by orthotopic transplantation of 2 tumor organoid lines in B6J or IL1R1 knockout hosts, as assessed by flow cytometry. Results show mean ± SEM of 5 biological replicates. **, $P < 0.01$, unpaired Student *t* test.

Having established that IL1α and TNFα are both secreted by cancer cells and sufficient to induce iCAF markers, we determined whether these NF-κB signaling activators are necessary for the induction of the iCAF phenotype. Neutralization of TNFα did not impair the induction of iCAF markers in PSCs cultured with tumor organoid–conditioned media (Supplementary Fig. S2D). However, targeting IL1α with a neutralizing antibody significantly reduced induction of iCAF marker genes and partially restored expression of myofibroblastic genes in PSCs exposed to tumor organoid–conditioned media (Fig. 2B). In addition, IL1α neutralization significantly impaired the proliferation of PSCs cultured as iCAFs, but not of PSCs cultured as myCAFs, suggesting that IL1α plays a key role in the iCAF phenotype (Fig. 2C; Supplementary Fig. S2E).

To confirm the role of tumor-secreted IL1α in establishing the iCAF phenotype, we used CRISPR/Cas9 to knock out IL1α in tumor organoids (Supplementary Fig. S2F). We cocultured these organoids with PSCs in transwells to model iCAFs, as previously described (ref. 19; Supplementary Fig. S1E). Levels of the iCAF markers were significantly reduced when PSCs were cultured with IL1α knockout organoids compared with Rosa26-targeted control organoids, whereas levels of the myCAF marker αSMA were significantly increased (Fig. 2D). As an orthogonal approach, to confirm that IL1 signaling is the major pathway responsible for iCAF formation *in vitro*, we knocked out IL1 receptor (IL1R1) in PSCs (Supplementary Fig. S2G). As expected, when PSCs were cultured in transwells with tumor organoids, levels of the iCAF markers were lower in IL1R1 knockout compared with Rosa26-targeted control PSCs, whereas myofibroblastic genes were higher (Fig. 2E). To confirm that the impaired acquisition of the iCAF phenotype was a direct consequence of IL1R1 deletion, we ectopically expressed guide-resistant IL1R1 constructs in three knockout clones (Supplementary Fig. S2H). Expression

of IL1R1 rescued the iCAF phenotype when PSCs were cultured with tumor organoid–conditioned media, confirming that IL1R1 is essential for the induction of iCAF markers (Supplementary Fig. S2I). Finally, we isolated two primary PSC lines from IL1R1 knockout mice (ref. 36; Supplementary Fig. S2J) and cultured them in the presence of IL1α. Contrary to what we observed in primary IL1R1 wild-type PSCs (Supplementary Fig. S2A), IL1α treatment did not promote the iCAF phenotype in primary IL1R1-deficient PSCs (Supplementary Fig. S2K). Altogether, these results support a key role of IL1 signaling in inducing the iCAF phenotype *in vitro*.

To investigate the role of IL1α in inducing the iCAF phenotype *in vivo*, we orthotopically transplanted Rosa26-targeted controls and three lines of IL1α-deficient tumor organoids in nu/nu mice to generate orthotopically grafted organoids (OGO; ref. 17). These three IL1α knockout lines showed different proliferative properties *in vitro* (Fig. 2F). Notably, all three lines of IL1α-deficient organoids formed significantly smaller tumors compared with control organoids (Fig. 2G). Collagen deposition and αSMA levels did not significantly differ between control OGOs and IL1α knockout OGOs (Supplementary Fig. S3A–S3D), suggesting there is no change in myofibroblastic CAFs *in vivo* in the absence of tumor-secreted IL1α. We then investigated whether the growth defect of IL1α knockout tumors is associated with a reduced presence of iCAFs in the PDAC microenvironment. We thus sorted CAFs from the tumors derived by transplants of the IL1α knockout organoid lines or Rosa26-targeted controls using EPCAM and PDGFRα/PDPN markers (Supplementary Fig. S1A). We then assessed the transcript level of inflammatory and myofibroblastic genes and observed a consistent reduction in *Il1a* and *Csf3* in CAFs of tumors derived from the knockout lines compared with the controls (Fig. 2H). The decrease in *Csf3* levels may be responsible for the reduced tumor growth observed *in vivo*, because G-CSF has been shown to be involved in PDAC progression (37, 38). However, this analysis showed only a partial response toward a less inflammatory CAF phenotype, suggesting that IL1α is not the only ligand that can induce iCAF formation *in vivo*. This agrees with the observation that IL1β and TNFα are also sufficient to induce an iCAF phenotype *in vitro* (Supplementary Fig. S2C) and have been shown to play a role in PDAC fibrosis (33, 34). In order to address the role of IL1β and TNFα *in vivo*, we sorted EPCAM$^+$ cells from OGOs of IL1α knockout organoids or Rosa26-targeted controls and assessed *Il1b* and *Tnf* transcript levels. Although *Il1b* transcript is undetectable in tumor organoids *in vitro*, it is expressed *in vivo* in the epithelial compartment of both controls and IL1α knockout tumors (Supplementary Fig. S3E). Similarly, *Tnf* expression was increased in epithelial cells of both controls and IL1α knockout tumors compared with organoids *in vitro* (Supplementary Fig. S3F). Altogether, these results demonstrate that deletion of tumor-derived IL1α impairs tumorigenesis and CAF expression of IL1α and G-CSF, but is not sufficient to fully prevent induction of an inflammatory stroma *in vivo*.

To circumvent the redundancy of IL1 isoforms and assess the role of IL1 signaling in inducing the iCAF phenotype *in vivo*, we orthotopically transplanted three tumor organoid lines in either IL1R1 knockout mice (36) or B6J controls. Quantification of collagen deposition and αSMA levels revealed a trend toward an increase of these parameters in tumors developed in IL1R1-deficient hosts (Supplementary Fig. S3G–S3J). In order to assess whether iCAF formation is impaired in the absence of IL1 signaling *in vivo*, we sorted CAFs from the OGOs using EPCAM and PDGFRα/PDPN markers (Supplementary Fig. S1A) and measured the transcript levels of inflammatory and myofibroblastic genes. iCAF markers were downregulated in CAFs sorted from tumors grown in IL1R1 knockout hosts compared with tumors grown in IL1R1 wild-type hosts, parallel to a modest, yet significant increase in myCAF marker gene-expression (Fig. 2I).

We then combined our previous flow cytometry strategy (Supplementary Fig. S1B) with flow-cytometric analysis of Ly6C, a surface marker that distinguishes a subset of iCAFs (Supplementary Fig. S1G, S3K, and S3L), to analyze myCAF and iCAF populations in tumors grown in IL1R1 knockout or wild-type hosts. In agreement with the analysis of transcript levels of inflammatory and myofibroblastic markers in CAFs (Fig. 2I), the results showed a decrease in Ly6C$^+$ iCAFs in tumors grown in IL1R1 knockout hosts compared with tumors grown in IL1R1 wild-type hosts (Fig. 2J; Supplementary Fig. S3M and S3N). Altogether, these results confirm a major role of tumor-secreted IL1 and stromal IL1R1 signaling in the formation of iCAFs *in vivo*.

IL1-Mediated Induction of Autocrine LIF in PSCs Activates JAK/STAT Signaling and Promotes iCAF Formation

To examine the downstream pathways activated by IL1 signaling that contribute to iCAF formation, we assessed the acute expression of inflammatory cytokines and chemokines, which are potential signaling effectors, in response to IL1α. Following exposure of PSCs to IL1α for 1 hour, iCAF marker genes were upregulated (Fig. 3A). A number of iCAF markers that are quickly induced by IL1α (e.g., IL6, G-CSF, and LIF) are known activators of the JAK/STAT signaling pathway (19, 21–23). In addition, the JAK/STAT transcriptional signature was previously found to be significantly upregulated in iCAFs compared with quiescent PSCs *in vitro* (19) and in iCAFs compared with myCAFs *in vivo* (Supplementary Fig. S1I). Accordingly, the JAK/STAT pathway members JAK1, JAK2, STAT3, and STAT1 were more highly activated in iCAFs compared with myCAFs and quiescent PSCs (Supplementary Fig. S4A). We therefore hypothesized that JAK/STAT signaling is involved in iCAF formation. We first assessed activation of the JAK/STAT pathway in response to IL1α and observed that treatment of quiescent PSCs with IL1α induces activation of JAK/STAT signaling (Fig. 3B). Moreover, neutralization of IL1α with an antibody significantly inhibited the JAK/STAT pathway in PSCs cultured with tumor organoid–conditioned media (Fig. 3C). Together, these results suggest that IL1α is both necessary and sufficient for JAK/STAT signaling activation in iCAFs. Accordingly, whereas conditioned media from Rosa26-targeted tumor organoids activated JAK/STAT signaling in PSCs as expected, conditioned media from IL1α knockout organoids were unable to activate the pathway (Fig. 3D).

To determine which activators of the JAK/STAT pathway promote the iCAF phenotype in an autocrine manner, we exposed PSCs to tumor organoid–conditioned media in which LIF, IL6, or G-CSF had been neutralized by antibodies,

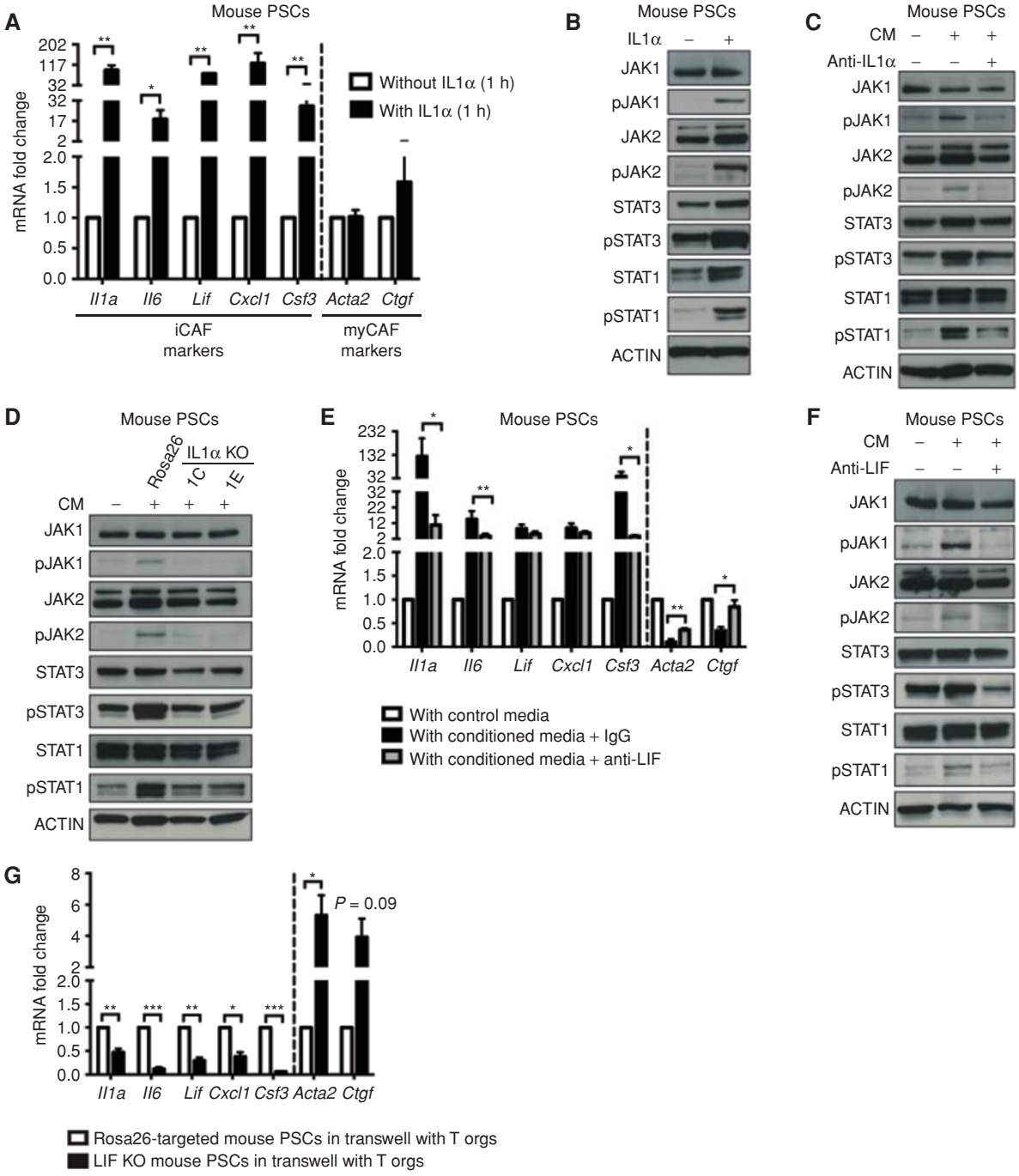

Figure 3. IL1-mediated induction of autocrine LIF in PSCs activates JAK/STAT signaling and promotes iCAF formation. **A,** qPCR analysis of iCAF (*Il1a, Il6, Lif, Cxcl1,* and *Csf3*) and myCAF (*Acta2* and *Ctgf*) markers in PSCs cultured in Matrigel in control media in the presence or absence of 1 ng/mL mouse IL1α for 1 hour. Results show mean ± SEM of 2 biological replicates. *, $P < 0.05$; **, $P < 0.01$, paired Student *t* test. **B,** Western blot analysis of pJAK1, JAK1, pJAK2, JAK2, pSTAT1, STAT1, pSTAT3, and STAT3 in PSCs cultured in Matrigel with control media in the presence or absence of 1 ng/mL mouse IL1α for 4 days. Loading control, ACTIN. **C,** Western blot analysis of pJAK1, JAK1, pJAK2, JAK2, pSTAT1, STAT1, pSTAT3, and STAT3 in PSCs cultured in Matrigel with control media or tumor organoid–conditioned media (CM) in the presence of a neutralizing antibody targeting IL1α or an IgG control for 4 days. Loading control, ACTIN. **D,** Western blot analysis of pJAK1, JAK1, pJAK2, JAK2, pSTAT1, STAT1, pSTAT3, and STAT3 in PSCs cultured in Matrigel with control media or tumor organoid–conditioned media from Rosa26-targeted controls or IL1α knockout (KO) tumor organoids for 4 days. Loading control, ACTIN. **E,** qPCR analysis of *Il1a, Il6, Lif, Cxcl1, Csf3, Acta2,* and *Ctgf* in PSCs cultured in Matrigel with control media or tumor organoid–conditioned media in the presence of a neutralizing antibody targeting LIF or an IgG control for 4 days. Results show mean ± SEM of 6 biological replicates. *, $P < 0.05$; **, $P < 0.01$, paired Student *t* test. **F,** Western blot analysis of pJAK1, JAK1, pJAK2, JAK2, pSTAT1, STAT1, pSTAT3, and STAT3 in PSCs cultured in Matrigel with control media or tumor organoid–conditioned media in the presence of a neutralizing antibody targeting LIF or an IgG control for 4 days. Loading control, ACTIN. **G,** qPCR analysis of *Il1a, Il6, Lif, Cxcl1, Csf3, Acta2,* and *Ctgf* in LIF knockout PSCs compared with Rosa26-targeted controls cultured in Matrigel in transwell with tumor organoids (T orgs) for 4 days. Results show mean ± SEM of 4 biological replicates. *, $P < 0.05$; **, $P < 0.01$; ***, $P < 0.001$, paired Student *t* test.

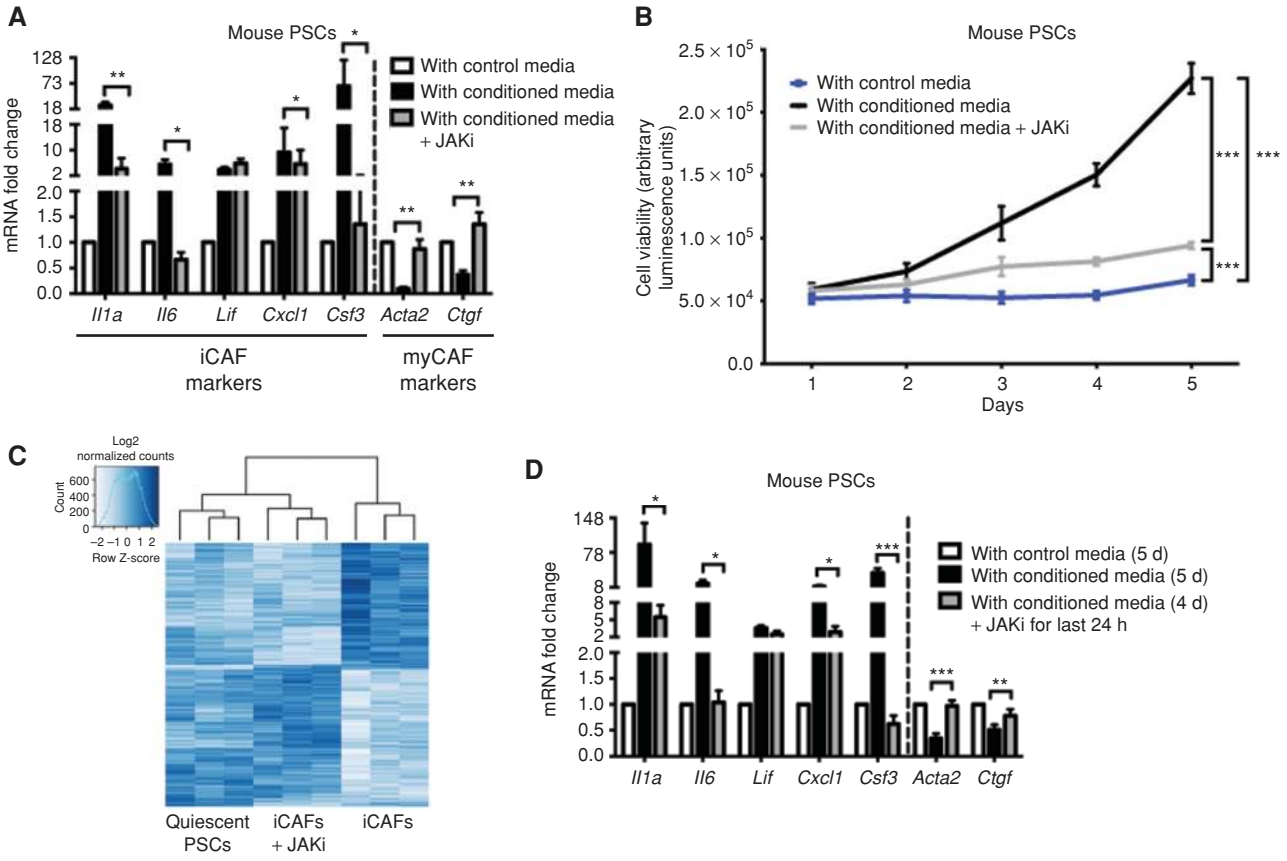

Figure 4. JAK/STAT signaling mediates the induction of the iCAF phenotype. **A,** qPCR analysis of iCAF (*Il1a, Il6, Lif, Cxcl1,* and *Csf3*) and myCAF (*Acta2* and *Ctgf*) markers in PSCs cultured in Matrigel with control media or tumor organoid–conditioned media in the presence or absence of 500 nmol/L JAK inhibitor (JAKi) AZD1480 for 4 days. Results show mean ± SEM of 5 biological replicates. *, $P < 0.05$; **, $P < 0.01$, paired Student *t* test. **B,** Proliferation curves of PSCs cultured in Matrigel with control media or tumor organoid–conditioned media in the presence or absence of 500 nmol/L JAKi. Results show mean ± SEM of 3 biological replicates. ***, $P < 0.001$, unpaired Student *t* test calculated for the last time point. **C,** RNA-sequencing analysis of quiescent PSCs ($n = 3$), iCAFs ($n = 3$), and iCAFs treated with 500 nmol/L JAKi for 4 days ($n = 3$). Color scheme of the heat map represents Z-score distribution. **D,** qPCR analysis of *Il1a, Il6, Lif, Cxcl1, Csf3, Acta2,* and *Ctgf* in PSCs cultured in Matrigel with control media or tumor organoid–conditioned media in the presence or absence of 500 nmol/L JAKi for the last 24 hours following 4 days in culture with conditioned media. Results show mean ± SEM of 5 biological replicates. *, $P < 0.05$; **, $P < 0.01$; ***, $P < 0.001$, paired Student *t* test. (*continued on following page*)

and assayed for activation of iCAF marker genes. Neutralization of LIF led to significant downregulation of the iCAF markers *Il1a, Il6,* and *Csf3*, with partial restoration of the myofibroblastic markers (Fig. 3E). Accordingly, treatment with a LIF-neutralizing antibody blocked activation of the JAK/STAT pathway (Fig. 3F), confirming that LIF has a major role in the activation of JAK/STAT signaling in iCAFs. In contrast, neutralization of G-CSF or IL6 did not reduce the expression of iCAF marker genes nor increase myCAF gene levels (Supplementary Fig. S4B and S4C), suggesting that these ligands are not major mediators of the iCAF phenotype. Accordingly, tumor organoid–conditioned media activated JAK/STAT signaling in IL6 knockout PSCs at levels comparable to PSC controls (Supplementary Fig. S4D). Together, our results support a model in which autocrine PSC-derived LIF induced downstream of IL1 signaling activates the JAK/STAT pathway and promotes the iCAF phenotype in PSCs. In support of this model, LIF could be detected in conditioned media from PSCs treated with IL1α (Supplementary Fig. S4E). To further confirm the role of autocrine LIF from PSCs in mediating induction of iCAF marker genes, we knocked out LIF in PSCs (Supplementary Fig. S4F). LIF deletion significantly impaired induction of iCAF marker genes in PSCs cultured in transwell with tumor organoids compared with Rosa26-targeted control PSCs (Fig. 3G). In addition, LIF deletion reduced JAK/STAT activation in PSCs exposed to tumor organoid–conditioned media (Supplementary Fig. S4G). Altogether, these results implicate autocrine LIF from PSCs as the major mediator of the inflammatory phenotype and JAK/STAT activation in iCAFs.

JAK/STAT Signaling Mediates the Induction of the iCAF Phenotype

Having established that tumor-derived IL1α induces JAK/STAT signaling through upregulation of LIF, and that LIF is involved in the induction of iCAF markers, we next wanted to determine whether JAK/STAT signaling per se is necessary for iCAF formation. To that end, we cultured PSCs with either IL1α or tumor organoid–conditioned media in the presence or absence of the JAK inhibitor AZD1480 (39). As expected, JAK inhibition prevented activation of JAK/STAT signaling in response to IL1α or tumor organoid–conditioned

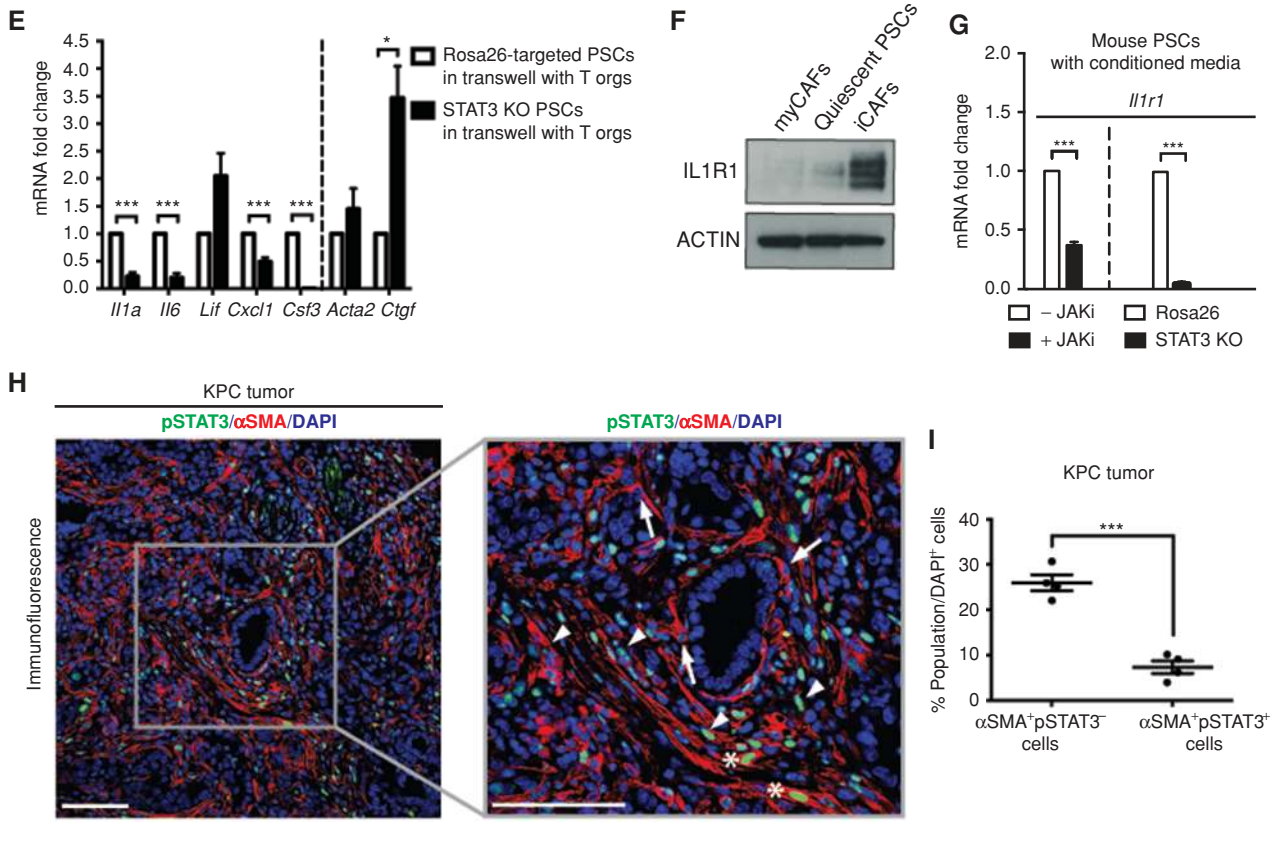

Figure 4. ***(Continued)*** **E,** qPCR analysis of *Il1a, Il6, Lif, Cxcl1, Csf3, Acta2,* and *Ctgf* in Rosa26-targeted controls and STAT3 knockout PSCs cultured in Matrigel in transwell with tumor organoids (T orgs) for 4 days. Results show mean ± SEM of 5 biological replicates. *, $P < 0.05$; ***, $P < 0.001$, paired Student *t* test. **F,** Western blot analysis of IL1R1 in myCAFs, quiescent PSCs, and iCAFs. Loading control, ACTIN. **G,** qPCR analysis of *Il1r1* in PSCs cultured in Matrigel with tumor organoid–conditioned media in the presence or absence of 500 nmol/L JAKi (left) and in STAT3 knockout (KO) PSCs compared with controls (right). Results show mean ± SEM of 4 and 5 biological replicates, respectively. ***, $P < 0.001$, paired Student *t* test. **H,** Representative immunofluorescence costains of pSTAT3 (green) and αSMA (red) in KPC tumor sections ($n = 4$). Counterstain, DAPI (blue). Arrows indicate examples of αSMA$^+$ pSTAT3$^-$ myCAFs; arrowheads indicate examples of αSMA$^-$ pSTAT3$^+$ cells; asterisks indicate examples of αSMA$^+$ pSTAT3$^+$ cells. Scale bars, 100 μm. **I,** Quantification of αSMA$^+$ pSTAT3$^-$ cells and αSMA$^+$ pSTAT3$^+$ cells in KPC tumor sections. Results show mean ± SEM of 4 biological replicates. ***, $P < 0.001$, unpaired Student *t* test.

media (Supplementary Fig. S5A and S5B). In addition, JAK inhibition significantly reduced the upregulation of iCAF markers and the downregulation of myCAF markers that occur in response to tumor organoid–conditioned media or IL1α (Fig. 4A; Supplementary Fig. S5A–S5D). Moreover, inhibition of JAK/STAT signaling led to profound impairment of the proliferation of PSCs cultured as iCAFs (Fig. 4B), while only modestly affecting the proliferation of PSCs cultured as myCAFs (Supplementary Fig. S5E). These results support a dominant role of JAK/STAT signaling in iCAF formation and are in line with the observation that JAK/STAT signaling is more active in iCAFs compared with myofibroblasts (Supplementary Fig. S4A). In addition, comparison of the expression profiles of quiescent PSCs and PSCs cultured as iCAFs in the presence or absence of the JAK inhibitor revealed that JAK inhibition *in vitro* maintains PSCs in a quiescent cell state (Fig. 4C; Supplementary Table S1). As expected, JAK/STAT and cytokine signaling pathways were downregulated following treatment with the JAK inhibitor by GSEA, whereas pathways characteristic of myofibroblasts, such as smooth muscle contraction and collagen formation, were significantly upregulated (Supplementary Fig. S5F). Impairment of the iCAF signature by inhibition of JAK/STAT signaling was not a consequence of a quiescent, nonproliferative state, as a 24-hour treatment with the JAK inhibitor was sufficient to block the expression of inflammatory genes and restore *Acta2* and *Ctgf* levels in established iCAFs (Fig. 4D; Supplementary Fig. S5G), without impairing their proliferation (Supplementary Fig. S5H). Altogether, these results indicate that, downstream of IL1 signaling, the JAK/STAT pathway is actively responsible for the iCAF phenotype.

In order to investigate which transcription factors in the JAK/STAT pathway promote iCAF formation, we independently deleted either STAT1 or STAT3 in PSCs. STAT1 loss did not significantly affect the expression of iCAF marker genes in PSCs cultured in transwell with tumor organoids compared with Rosa26-targeted controls (Supplementary Fig. S5I and S5J). In contrast, STAT3 knockout PSCs showed significantly reduced expression of iCAF marker genes with increased *Ctgf* levels when cultured in transwell with tumor organoids (Fig. 4E; Supplementary Fig. S5K). To corroborate a role for STAT3 in regulating iCAF marker genes, we

performed DNA motif analysis on the promoters of genes differentially expressed between myofibroblasts and iCAFs in our previous RNA-sequencing data set (19). Indeed, STAT3 motifs were enriched in the promoters of a number of iCAF genes, including the promoters of *Il6* and *Csf3* ($P < 0.001$; Supplementary Table S1). Moreover, analysis of ENCODE human STAT3 chromatin immunoprecipitation coupled with high-throughput deep sequencing (ChIP-seq) data sets (UCSC browser) confirmed STAT3 binding at these promoters (40).

STAT3 motifs were also identified in the promoters of both mouse and human *IL1R1* genes ($P < 0.001$; Supplementary Table S1), and ENCODE human STAT3 ChIP-seq data sets (UCSC browser) revealed STAT3 binding at the *IL1R1* promoter (40). Accordingly, IL1R1 expression was significantly upregulated in iCAFs compared with myCAFs (Fig. 4F; Supplementary Fig. S5L), whereas it was significantly downregulated in PSCs where STAT3 was knocked out or in PSCs cultured with tumor organoid–conditioned media in the presence of the JAK inhibitor (Fig. 4G; Supplementary Fig. S5M and S5N). These results support the presence of a positive feedback loop whereby the iCAF phenotype is maintained through IL1-dependent activation of JAK/STAT signaling, which in turn leads to the upregulation of IL1R1 expression.

Our data indicate that JAK/STAT signaling promotes an iCAF phenotype *in vitro*. To determine whether JAK/STAT signaling is active in iCAFs *in vivo*, we performed immunofluorescence costaining of phosphorylated STAT3 (pSTAT3) and αSMA in KPC tumors and human PDAC. Levels of pSTAT3 were found to be low in αSMA-positive myCAFs surrounding the tumor cells (Fig. 4H; Supplementary Fig. S5O, arrows). Whereas a small number of αSMA-positive, pSTAT3-positive myofibroblasts could be detected (Fig. 4H; Supplementary Fig. S5O, asterisk), multiple αSMA-negative, pSTAT3-positive cells were located in the stroma farther away from tumor cells (Fig. 4H; Supplementary Fig. S5O, arrowheads). This analysis showed a significantly higher number of pSTAT3-negative myofibroblasts compared with pSTAT3-positive αSMA-positive cells (Fig. 4I; Supplementary Fig. S5P), demonstrating that JAK/STAT signaling is low in myCAFs in mouse and human PDAC.

TGFβ Signaling Antagonizes IL1-Induced JAK/STAT Signaling and Inhibits the iCAF Phenotype

Although we have shown that iCAF formation is dependent upon tumor-secreted IL1 that activates a LIF/JAK/STAT-dependent cytokine cascade, the mechanisms underlying myCAF biology remain unknown. We hypothesized that myCAF formation could be dependent on juxtacrine signals or paracrine signals that are produced by adjacent tumor cells. Previous expression analysis identified enrichment of TGFβ target genes in the myCAF signature compared with quiescent PSCs and iCAFs (19). Given that TGFβ is known to promote a myofibroblastic phenotype (41, 42), we investigated whether TGFβ signaling could be a dominant feature in this CAF subtype.

To measure TGFβ signaling in the various CAF populations, we prepared cellular and nuclear protein extracts from PSCs cultured as quiescent PSCs, iCAFs, or myCAFs and evaluated activation of the TGFβ pathway. As expected, PSCs cultured as myCAFs had increased expression of the myofibroblastic marker αSMA (Fig. 5A). In addition, whereas the levels of total SMAD2 and SMAD3, two effectors of TGFβ signaling, were comparable in different PSC states, myCAFs had elevated levels of active phosphorylated SMAD2 and SMAD3 (pSMAD2 and pSMAD3) and of the TGFβ target gene CTGF (Fig. 5A). Moreover, myCAFs had increased nuclear localization of the TGFβ effector SMAD4 compared with quiescent PSCs and iCAFs (Fig. 5B), indicative of active TGFβ signaling. Consistent with these observations, TGFβ treatment of PSCs cultured in Matrigel in control media did not induce the iCAF phenotype (Supplementary Fig. S6A). On the contrary, TGFβ induced the expression of TGFβ-responsive genes (e.g., *Ctgf* and *Col1a1*) and promoted PSC proliferation and morphologic changes, in agreement with previous literature (refs. 41, 42; Supplementary Fig. S6A–S6C). Accordingly, single-cell RNA-sequencing analysis of KPC tumors confirmed higher expression of TGFβ-responsive genes in myCAFs compared with iCAFs *in vivo* (Fig. 5C). Moreover, immunofluorescence of pSMAD2 and E-cadherin (ECAD) showed increased pSMAD2 levels in cells proximal to ECAD-positive epithelial cells compared with distal areas in KPC tumors (Supplementary Fig. S6D). Finally, immunofluorescence costain of pSMAD2 and αSMA in KPC tumors and human PDAC showed an elevated number of pSMAD2/αSMA double-positive myofibroblasts (Fig. 5D; Supplementary Fig. S6E), which represented the majority of pSMAD2-positive cells (Fig. 5E; Supplementary Fig. S6F). Altogether, these results suggest that TGFβ signaling is active in myCAFs in mouse and human PDAC.

As tumor-secreted IL1 should be able to signal to both the distally located iCAFs and the tumor-proximal myCAFs,

Figure 5. TGFβ signaling antagonizes IL1-induced JAK/STAT signaling and inhibits the iCAF phenotype. **A,** Western blot analysis of SMAD2, pSMAD2, pSMAD3, SMAD3, CTGF, and αSMA in myCAFs (myC), quiescent PSCs (qP), and iCAFs (iC). Loading control, HSP90α. **B,** Western blot analysis of the TGFβ signaling effector SMAD4 following nuclear fractionation of quiescent PSCs (qP), iCAFs (iC), and myCAFs (myC). Loading controls, HSP90α (cytoplasmic fractions) and H3 (nuclear fractions). The same amount of protein lysate was loaded in each lane. **C,** Violin plots showing single-cell RNA-sequencing analysis of *Ctgf* and *Col1a1* of a representative KPC tumor ($n = 2$) in myCAFs (blue) and iCAFs (orange). **D,** Representative immunofluorescence costains of pSMAD2 (green) and αSMA (red) in KPC tumor sections ($n = 5$). Counterstain, DAPI (blue). Arrowheads indicate examples of αSMA^+ $pSMAD2^+$ cells. Scale bars, 100 μm. **E,** Quantification of $pSMAD2^+$ αSMA^- cells and $pSMAD2^+$ αSMA^+ cells in KPC tumor sections. Results show mean ± SEM of 5 biological replicates. **, $P < 0.01$, paired Student *t* test. **F,** qPCR analysis of iCAF (*Il1a, Il6, Lif, Cxcl1,* and *Csf3*) and myCAF (*Acta2* and *Ctgf*) markers in PSCs cultured in Matrigel with control media or tumor organoid–conditioned media in the presence or absence of 20 ng/mL mouse TGFβ for 4 days. Results show mean ± SEM of 6 biological replicates. **, $P < 0.01$; ***, $P < 0.001$, paired Student *t* test. **G,** Western blot analysis of pJAK1, JAK1, pJAK2, JAK2, pSTAT1, STAT1, pSTAT3, STAT3, pSMAD2, CTGF, and αSMA in PSCs cultured in Matrigel with control media or tumor organoid–conditioned media (CM) in the presence or absence of 20 ng/mL mouse TGFβ for 4 days. Loading control, ACTIN. **H,** Proliferation curves of PSCs cultured in Matrigel with control media or tumor organoid–conditioned media in the presence or absence of 20 ng/mL mouse TGFβ. Results show mean ± SD of 5 technical replicates. *, $P < 0.05$; **, $P < 0.01$; ***, $P < 0.001$, unpaired Student *t* test calculated for the last time point. **I,** qPCR analysis of *Il1r1* in PSCs cultured in Matrigel with control media or tumor organoid–conditioned media in the presence or absence of 20 ng/mL mouse TGFβ for 4 days. ***, $P < 0.001$, paired Student *t* test. **J,** Western blot analysis of IL1R1 in PSCs cultured in Matrigel with control media or tumor organoid–conditioned media in the presence or absence of 20 ng/mL mouse TGFβ for 4 days. Loading control, ACTIN.

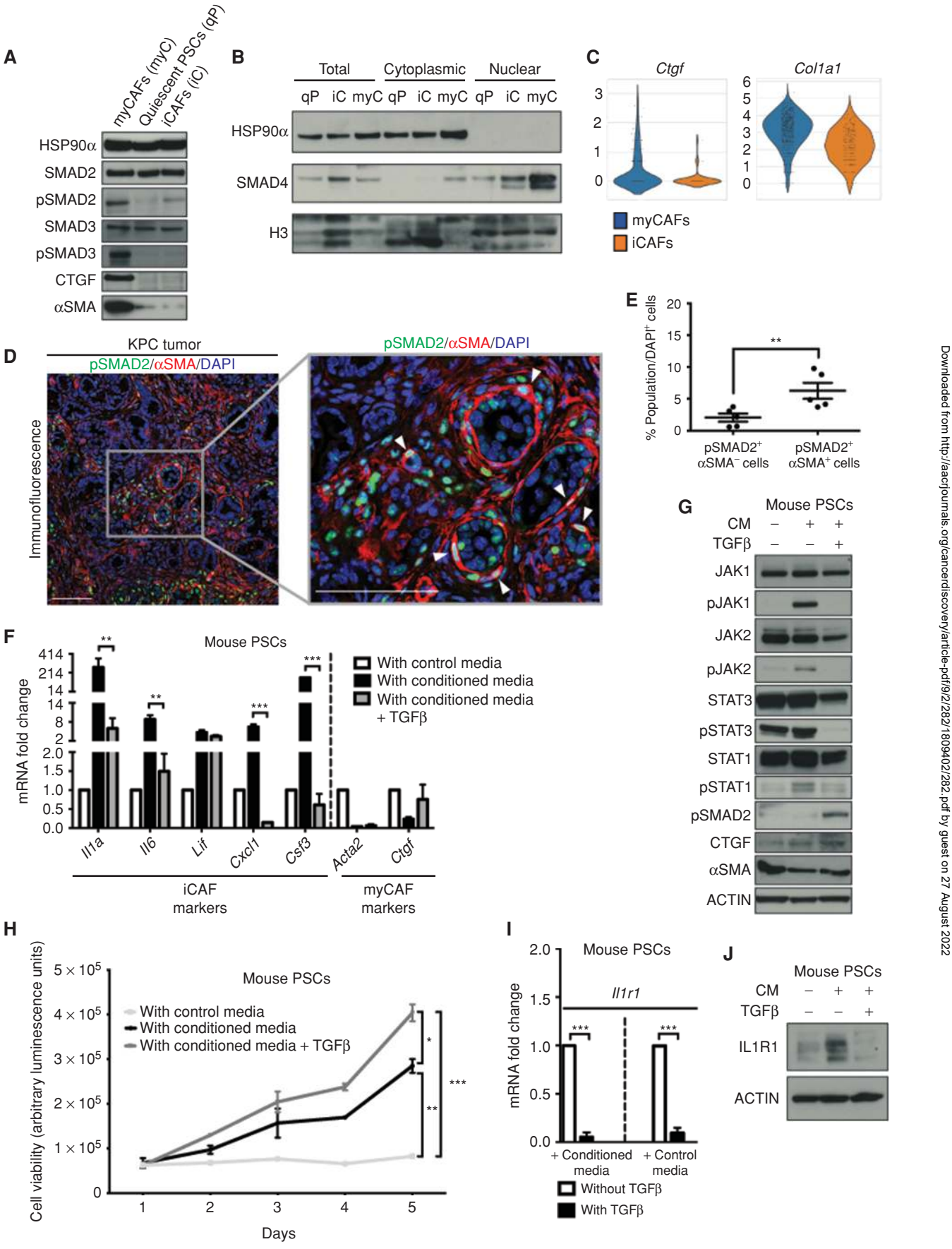

we reasoned that in myCAFs some other signaling pathway likely prevents the induction of an inflammatory phenotype. Accordingly, the observation that nuclear pSTAT3 is rarely found in αSMA-positive myCAFs surrounding cancer cells (Fig. 4H) is consistent with a role for tumor-proximal paracrine or juxtacrine signaling in preventing JAK/STAT activation and the iCAF phenotype. Given that TGFβ signaling is more active in myCAFs compared with iCAFs (Fig. 5A–C), we tested whether TGFβ signaling might be responsible for the inhibition of the iCAF phenotype in myCAFs. Indeed, treatment of PSCs cultured to form iCAFs with the TGFβ pathway inhibitor A83-01 led to increased expression of iCAF marker genes (Supplementary Fig. S6G). Moreover, congruent with the hypothesis that TGFβ signaling inhibits iCAF formation, the addition of TGFβ to tumor organoid–conditioned media or to media containing IL1α significantly reduced the expression of iCAF markers and partially increased myofibroblastic markers in mouse and human PSCs (Fig. 5F; Supplementary Fig. S6H and S6I). Accordingly, the addition of TGFβ blocked the activation of JAK/STAT signaling in PSCs cultured with tumor organoid–conditioned media or IL1α (Fig. 5G; Supplementary Fig. S6J), suggesting that the downregulation of iCAF gene expression observed is a consequence of TGFβ-mediated inhibition of the JAK/STAT pathway. Proliferation assays showed that myCAFs proliferate faster than iCAFs *in vitro* (Supplementary Fig. S6K). Consistent with the hypothesis that TGFβ shifts the iCAF phenotype to a more myofibroblastic state, the proliferation rate of PSCs cultured with tumor organoid–conditioned media containing TGFβ was higher than PSCs cultured in conditioned media alone (Fig. 5H).

We have shown that JAK/STAT signaling positively regulates the expression of IL1R1 (Fig. 4G; Supplementary Fig. S5M and S5N). To further investigate the molecular mechanism behind TGFβ and JAK/STAT pathway antagonism in the context of CAF heterogeneity in PDAC, we performed DNA motif analysis and found, in addition to STAT3 motifs, SMAD2/3/4 motifs in the promoters of both mouse and human *Il1R1* genes ($P < 0.001$; Supplementary Table S1). In addition, analysis of human SMAD3 ChIP-seq data sets confirmed SMAD3 binding at the *IL1R1* promoter (43). We therefore hypothesized that TGFβ antagonizes JAK/STAT signaling by directly repressing *Il1r1* expression and thus blocking the cytokine cascade triggered downstream of IL1R1 activation. To test our hypothesis, we measured *Il1r1* expression levels following TGFβ treatment in PSCs cultured with control media or tumor organoid–conditioned media and demonstrated that TGFβ treatment significantly reduced IL1R1 expression (Fig. 5I and J). Similar results were obtained with mouse and human PSCs cultured with both IL1α and TGFβ (Supplementary Fig. S6L and S6M). Altogether, these data suggest that TGFβ prevents activation of the iCAF phenotype by removing the receptor that would activate the cascade that leads to iCAF formation.

TGFβ Signaling Inhibition Targets myCAFs *In Vivo*

We have shown that SMAD2 is active in myofibroblasts *in vivo* (Fig. 5D and E; Supplementary Fig. S6E and S6F). To further evaluate the role of TGFβ signaling in myCAFs *in vivo*, we treated tumor-bearing KPC mice for 10 days with the TGFβ receptor (TGFBR) inhibitor galunisertib (LY2157299; ref. 44). Assessment of pSMAD2 levels confirmed effective targeting of the TGFβ pathway (Supplementary Fig. S7A and S7B). Treated mice showed a nonsignificant reduction in tumor cell proliferation (Supplementary Fig. S7C and S7D), and no change in tumor growth (Fig. 6A). Additionally, although galunisertib did not significantly increase the iCAF content of treated KPC mice (Supplementary Fig. S7E and S7F), stromal content was modestly, yet significantly, reduced, demonstrating attenuation of myCAF properties, as shown by the analysis of collagen deposition (Fig. 6B–D) and αSMA levels (Fig. 6E and F). Our results collectively support a key role of the TGFβ pathway in myofibroblasts *in vivo*.

JAK Inhibition Shifts iCAFs to a Myofibroblastic Phenotype *In Vivo*

Finally, to determine the role of JAK/STAT signaling in CAFs *in vivo*, we treated tumor-bearing KPC mice with the JAK inhibitor AZD1480 for 10 days. Assessment of pSTAT3 levels confirmed inhibition of the JAK/STAT pathway (Supplementary Fig. S8A and S8B). Contrary to what was observed following inhibition of TGFβ signaling, tumor volume analysis revealed a significant decrease in tumor growth following treatment with the JAK inhibitor compared with vehicle (Fig. 7A). This reduction in tumor growth was associated with impaired proliferation of cancer cells in the treated tumors, as shown by quantification of phospho histone H3 (pH3) levels (Supplementary Fig. S8C and S8D). Histologically, this treatment led to a significant increase in collagen deposition (Fig. 7B–D). Flow cytometry analysis of KPC tumors using our previously described strategy (Supplementary Fig. S1B) also revealed increased abundance of CAFs in JAK inhibitor–treated tumors compared with vehicle controls (Fig. 7E; Supplementary Fig. S8E). Moreover, KPC tumors from mice treated with the JAK inhibitor had increased levels of αSMA (Fig. 7F and G), suggesting that JAK inhibition may promote a shift in the CAF population from an iCAF phenotype toward a more myofibroblastic state.

We previously showed that myCAFs proliferate faster than iCAFs *in vitro* (Supplementary Fig. S6K). To explain the increased CAF abundance in JAK inhibitor–treated tumors compared with vehicle controls, and considering that JAK inhibition seems to promote formation of myofibroblasts, we investigated whether myCAFs proliferate more than iCAFs *in vivo*. Single-cell RNA-sequencing analysis of iCAFs and myCAFs in KPC tumors showed higher expression of the cell-cycle genes *Cks2* and *Ccnb2* and of the proliferation marker *Mki67* in myCAFs relative to iCAFs (Supplementary Fig. S8F). Moreover, we used our flow cytometry strategy with the iCAF marker Ly6C (Supplementary Fig. S3K and S3L) to analyze the cell proliferation of CAFs in 5-Ethynyl-2-deoxyuridine (EdU)–labeled KPC tumors. A greater number of $Ly6C^-$ CAFs incorporated EdU compared with $Ly6C^+$ iCAFs, suggesting that myCAFs are more proliferative (Fig. 7H). Altogether, these data provide an explanation for the increased CAF abundance observed in JAK inhibitor–treated KPC tumors (Fig. 7E; Supplementary Fig. S8E).

To confirm that JAK inhibition increased the number of myofibroblasts, we used the Ly6C-based flow cytometry approach to quantify iCAF and myCAF populations in vehicle- or JAK inhibitor–treated KPC tumors. The results

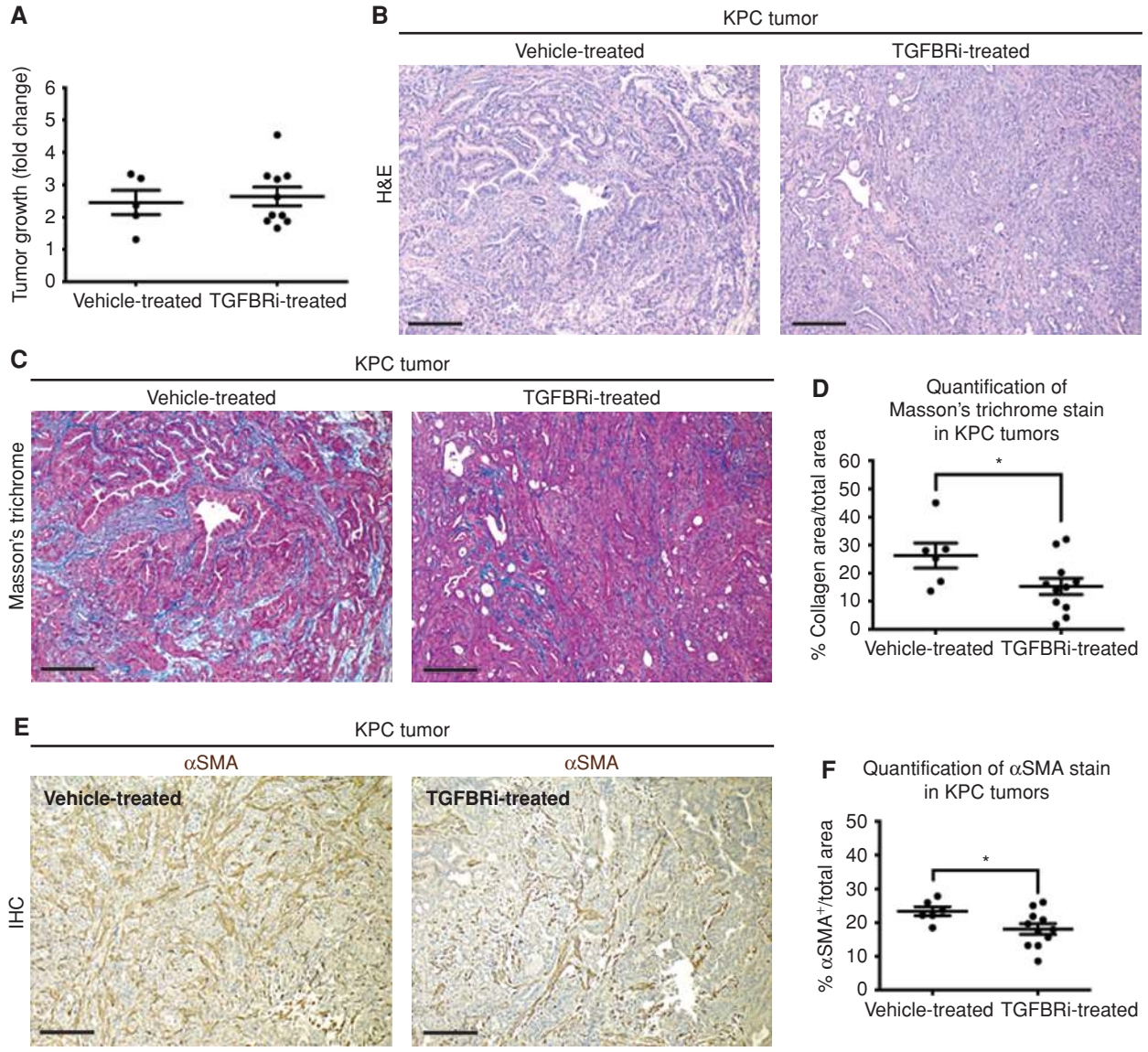

Figure 6. Inhibition of TGFβ signaling targets myofibroblasts *in vivo*. **A,** Tumor volume analysis based on ultrasound measurements of vehicle- and TGFBR inhibitor (TGFBRi)–treated KPC tumors. Results show mean ± SEM of 5 and 10 tumors, respectively. No statistical difference was found, as calculated by unpaired Student *t* test. **B,** Representative hematoxylin and eosin (H&E) stain of vehicle- and TGFBRi-treated KPC tumor sections ($n = 6$ and 11, respectively). Scale bars, 200 μm. **C,** Representative Masson's trichrome stain of vehicle- and TGFBRi-treated KPC tumor sections ($n = 6$ and 11, respectively). Scale bars, 200 μm. **D,** Quantification of Masson's trichrome stain in vehicle- and TGFBRi-treated KPC tumors. Results show mean ± SEM of 6 and 11 biological replicates, respectively. *, $P < 0.05$, unpaired Student *t* test. **E,** Representative IHC of αSMA stain of vehicle- and TGFBRi-treated KPC tumor sections ($n = 6$ and 11, respectively). Scale bars, 200 μm. **F,** Quantification of αSMA stain in vehicle- and TGFBRi-treated KPC tumors. Results show mean ± SEM of 6 and 11 biological replicates, respectively. *, $P < 0.05$, unpaired Student *t* test.

demonstrated reduced presence of Ly6C$^+$ iCAFs in JAK inhibitor–treated tumors compared with vehicle controls (Fig. 7I; Supplementary Fig. S8G and S8H), further supporting a role for JAK inhibition in modulating the PDAC microenvironment by shifting iCAFs toward a more myofibroblastic state.

Altogether, our data support a model in which pathway antagonism between JAK/STAT and TGFβ signaling acts to define CAF heterogeneity in PDAC. In particular, tumor-secreted TGFβ acts locally on adjacent myCAFs, downregulating the expression of IL1R1, thereby preventing the IL1-dependent activation of JAK/STAT signaling. Ultimately, this prevents induction of the iCAF phenotype in tumor-proximal myCAFs. Furthermore, TGFβ, which is secreted as a latent form and likely sequestered by the extracellular matrix, cannot act on CAFs located distally from tumor glands, leading to increased IL1R1 expression in these distal CAFs. This allows tumor-secreted IL1 to stimulate a cytokine cascade following activation of NF-κB signaling that, predominantly through autocrine LIF, activates the JAK/STAT pathway in CAFs. JAK/STAT signaling then maintains the inflammatory CAF phenotype through a positive feedback loop involving STAT3-mediated upregulation of IL1R1 (Fig. 7J).

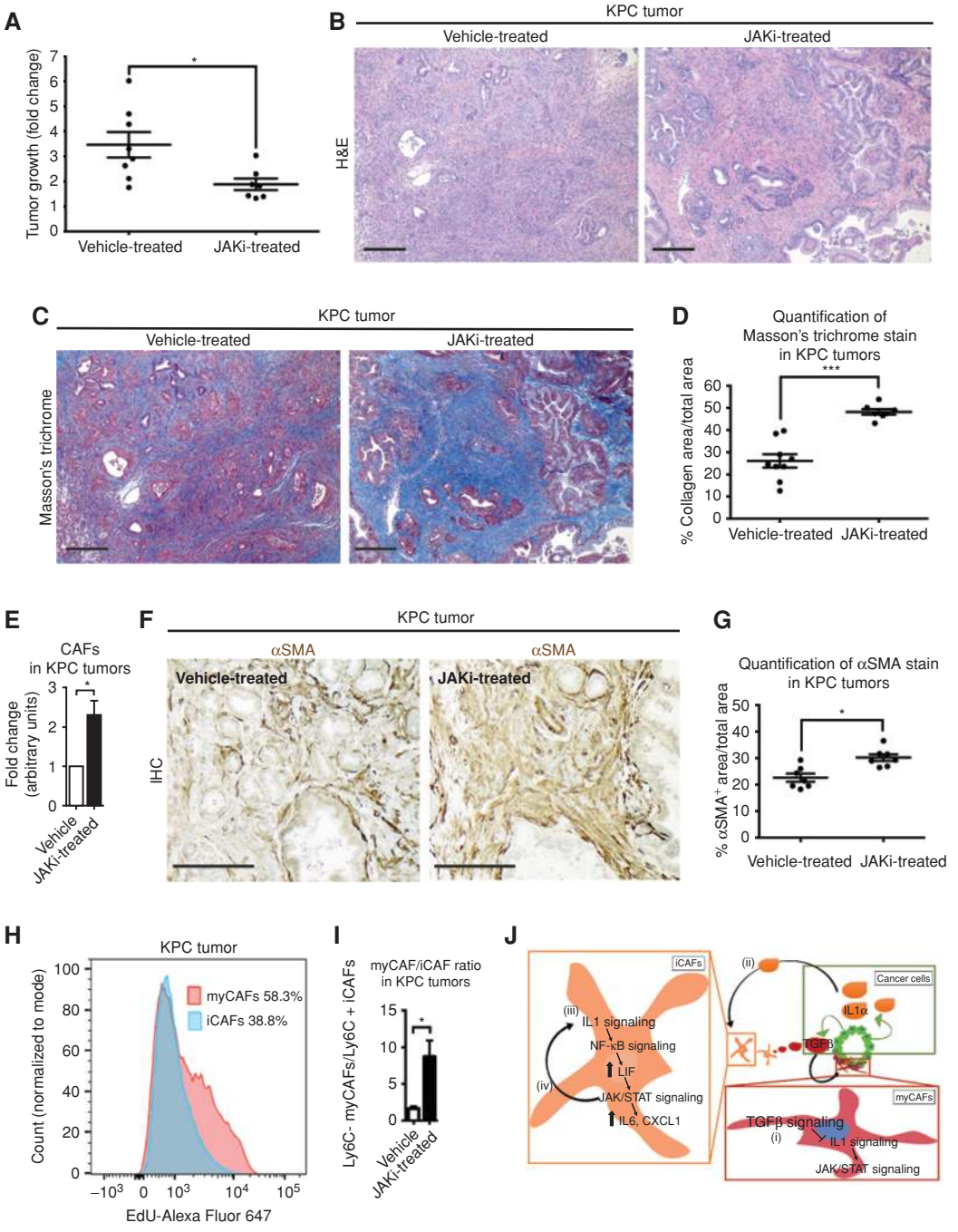

Figure 7. JAK inhibition shifts iCAFs to a myofibroblastic phenotype *in vivo*. **A,** Tumor volume analysis based on ultrasound measurements of vehicle- and JAK inhibitor (JAKi)–treated KPC tumors. Results show mean ± SEM of 8 and 7 tumors, respectively. *, $P < 0.05$, unpaired Student *t* test. **B,** Representative hematoxylin and eosin (H&E) stain of vehicle- and JAKi-treated KPC tumor sections ($n = 9$ and 7, respectively). Scale bars, 200 μm. **C,** Representative Masson's trichrome stain of vehicle- and JAKi-treated KPC tumor sections ($n = 9$ and 7, respectively). Scale bars, 200 μm. **D,** Quantification of Masson's trichrome stain in vehicle- and JAKi-treated KPC tumors. Results show mean ± SEM of 9 and 7 biological replicates, respectively. ***, $P < 0.001$, unpaired Student *t* test. **E,** Quantification of CAFs in vehicle- and JAKi-treated KPC tumors, as assessed by flow cytometry. Results show mean ± SEM of 4 biological replicates. *, $P < 0.05$, unpaired Student *t* test. **F,** Representative IHC of αSMA stain of vehicle- and JAKi-treated KPC tumor sections ($n = 7$). Scale bars, 200 μm. **G,** Quantification of αSMA stain in vehicle- and JAKi-treated KPC tumors. Results show mean ± SEM of 7 biological replicates. *, $P < 0.05$, unpaired Student *t* test. **H,** Representative flow-cytometric analysis of iCAFs and myCAFs in EdU-treated KPC tumors ($n = 2$). The values shown represent the EdU+ cells in each CAF population. **I,** Quantification of Ly6C- myCAF/Ly6C+ iCAF ratio in vehicle- and JAKi-treated KPC tumors, as assessed by flow cytometry. Results show mean ± SEM of 3 biological replicates. *, $P < 0.05$, unpaired Student *t* test. **J,** Model explaining the pathway antagonism that determines iCAF and myCAF formation in PDAC. (i) Tumor-secreted TGFβ activates TGFβ signaling in adjacent myCAFs, preventing induction of the iCAF phenotype by suppressing IL1R1 expression. (ii) Conversely, tumor-secreted IL1 activates IL1 signaling in CAFs that are located farther away from tumor glands. (iii) In these CAFs, IL1 signaling induces a cytokine cascade that leads to JAK/STAT signaling activation through NF-κB signaling and autocrine LIF. (iv) The activated JAK/STAT pathway establishes a positive feedback loop by upregulating IL1R1 expression.

DISCUSSION

Here, we identified TGFβ and IL1/JAK/STAT signaling as the major pathways responsible for myCAF and iCAF formation in mouse and human PDAC. Notably, GSEA of iCAF and myCAF populations that have been identified by single-cell RNA sequencing in human PDAC samples has confirmed that the JAK/STAT pathway is significantly upregulated in iCAFs compared with myCAFs (E. Elyada and colleagues, in preparation). Additionally, in agreement with our previous work (19), we identified a minor population of αSMA/pSTAT3 double-positive cells by immunofluorescence. These cells might represent an additional subtype of CAFs or an intermediate state between the iCAF and myCAF phenotypes, further supporting the plasticity between these two CAF populations *in vivo* and recapitulating what was observed *in vitro* (19). We suggest that iCAFs and myCAFs are indeed interconvertible cell states, rather than endpoints in differentiation, depending on their location within the tumor and on the tumor-derived cues they are exposed to. This could direct the design of treatment strategies meant to convert potential tumor-promoting CAFs into tumor-restraining CAF populations. The secretory phenotype of iCAFs suggests a role for this CAF subtype in promoting tumor progression and cancer-associated systemic effects, such as cachexia and immune suppression (6, 9, 11, 21–24, 38, 45, 46). The benefits of targeting iCAFs would be 2-fold: depleting iCAFs would reduce the secretion of tumor-promoting cytokines and chemokines, and shifting iCAFs to a more myofibroblastic state would increase the αSMA-positive CAF population that has been previously suggested to restrain tumor progression (14, 16). Accordingly, JAK inhibition significantly increased the myCAF/iCAF ratio in treated tumors. This was also reflected in an extensive deposition of extracellular matrix, a feature attributed to myCAFs based on their transcriptional profile. This matrix by acting as a barrier to drug delivery would offer a potential explanation for the poor outcome observed in clinical trials using JAK inhibitors with chemotherapy (47, 48). Whereas the dramatic changes in stromal composition that we observed were not reported previously (49, 50), the different genetics of the PDAC mouse models used might explain this discrepancy. Moreover, although we observed only a modest increase in collagen deposition and αSMA levels in orthotopic tumors grown in the IL1R1 knockout mouse model compared with control mice, this may reflect the overall diminished stromal content in this model compared with the KPC mouse model.

Our studies suggest the potential of novel therapeutic combinations to selectively modulate the PDAC stroma by targeting potential tumor-promoting components, such as iCAFs, along with components that impede drug delivery, such as myCAF-derived desmoplasia (2, 4, 5). The potential benefit of targeting iCAFs in PDAC is supported by the observation that a 10-day treatment with the JAK inhibitor in KPC mice led to a significant reduction in cell proliferation and tumor growth, parallel to an increase in the proportion of CAFs as myofibroblasts. On the contrary, TGFBR inhibition did not reduce tumor growth, while partially attenuating the function of myCAFs, suggesting that distinct CAF populations impart differential outcomes on PDAC progression. Although we cannot exclude that these effects on CAF populations are also partially a consequence of direct targeting of cancer cells, these results show differential responses of KPC tumors to drugs that impair the iCAF or myCAF phenotype.

Alternative approaches to target the iCAF population are suggested by the identification of IL1 signaling as the initiator of the cytokine cascade that leads to JAK/STAT activation. Previous studies have reported a role of tumor-secreted IL1 in remodeling PDAC stroma (32, 33). In particular, IL1α has been shown to induce the expression of inflammatory factors, such as IL6 and CXCL8, in PDAC CAFs *in vitro*, although no downstream mechanism has been reported (32). Targeting IL1 signaling in PDAC mouse models with the IL1 receptor antagonist anakinra has shown a role for this pathway in cancer cells in PDAC progression (31), and these preclinical studies have encouraged an early phase I clinical trial in combination with standard chemotherapy in PDAC (NCT02021422). Although the effects of IL1 signaling inhibition in PDAC have been attributed to the role of this pathway in cancer cells, our data suggest that the benefits of the IL1 receptor antagonist might also depend on targeting of the inflammatory stroma. We have identified the IL1 pathway in a subset of CAFs that, in addition to being uniquely characterized by an inflammatory signature, also presents a lack of myofibroblastic features. The combination of these traits might be important for the function of this CAF subtype. In addition, because we demonstrated that LIF is a key mediator of the mechanism that leads to iCAF formation, targeting of the iCAF population might also be achieved by *in vivo* neutralization of LIF. Finally, we have demonstrated that TNFα has the potential of inducing iCAFs, and therefore a combinatorial therapy with both a TNFα-neutralizing antibody and the IL1 receptor antagonist might be necessary for more effective targeting of iCAFs *in vivo*.

Altogether, our observations support a model for myCAF and iCAF formation in which tumor-secreted TGFβ acts locally on the adjacent myCAFs and antagonizes tumor-secreted IL1 activity and the JAK/STAT pathway. Pathway antagonism between TGFβ and STAT activation has been previously suggested in the context of epithelial cells (51, 52). We have now uncovered a role of TGFβ in blocking JAK/STAT signaling in CAFs, and we present evidence that this antagonism depends on their opposite effects on IL1R1 expression. Our study thus explains the mutual exclusivity and plasticity of iCAF and myCAF populations and provides a platform for further investigation of their role in PDAC progression by selective therapeutic or genetic targeting of each population.

METHODS

Mouse Models

KPC (*Kras*$^{LSL\text{-}G12D/+}$; *Trp53*$^{LSL\text{-}R172H/+}$; *Pdx1*-Cre) mice were previously described (18). C57BL/6J (stock number 000664) and IL1R1 knockout (ref. 36; stock number 003245) mice were purchased from The Jackson Laboratory; nu/nu mice (stock number 24102242) were purchased from The Charles River Laboratory. All animal procedures and studies were conducted in accordance with the Institutional Animal Care and Use Committee at Cold Spring Harbor Laboratory (CSHL).

Cell Lines and Cell Culture

Mouse PSCs, KPC primary tumor cells, and tumor and metastatic pancreatic organoid lines were previously described (17, 19). Primary mouse IL1R1 knockout PSCs were isolated by IL1R1 knockout mice, as previously described (19). Human PSCs were purchased from ScienCell (3830). Mouse PSCs, human PSCs, NIH-3T3 fibroblasts (available at CSHL) and KPC primary tumor cells were cultured in DMEM (10-013-CV; Fisher Scientific) containing 5% FBS. All cells were cultured for no more than 20 to 25 passages at 37°C with 5% CO_2. For conditioned media experiments, tumor organoids were cultured for 3 to 4 days in DMEM with 5% FBS. For transwell cultures, organoids were plated on top of transwell membranes (82051-572; VWR) with PSCs growing in Matrigel (356231; Corning) in 24-well plates in DMEM with 5% FBS. Cell lines were characterized by flow cytometry. Cell line authentication was not performed. *Mycoplasma* testing with the MycoAlert Mycoplasma Detection Kit (LT07-318; Lonza) is performed monthly at our institution, and each cell line has been tested at least once after thawing or isolation, and retested prior to RNA sequencing and orthotopic transplantation experiments.

Drug and Antibody Treatments

Cells were treated with 0.1 or 1 ng/mL mouse (400-ML-005/CF; R&D Systems) or human (200-LA-002/CF; R&D Systems) IL1α, 1 ng/mL mouse IL1β (401-ML-005/CF; R&D Systems), 10 ng/mL mouse TNFα (410-MT-010/CF; R&D Systems), 20 ng/mL mouse (7666-MB-005/CF; R&D Systems) or human TGFβ1 (T7039-2UG; Sigma), 500 nmol/L JAK inhibitor AZD1480 (S2162; Selleckchem), 30 μmol/L IKKβ inhibitor ML102B, 1 μmol/L A83-01 (2939; Tocris Bioscience), 3 μg/mL IL1α-neutralizing antibody (MAB4001; R&D Systems) or an IgG control (400902; BioLegend), 5 μg/mL TNFα-neutralizing antibody (11969S; Cell Signaling Technology) or an IgG control (sc-2027; Santa Cruz), 3.4 μg/mL LIF-neutralizing antibody (AF449; R&D Systems) or an IgG control (AB-108-C; R&D Systems), 3.8 μg/mL G-CSF- (MAB414; R&D Systems), or IL6- (MAB406; R&D Systems) neutralizing antibodies or an IgG control (MAB005; R&D Systems).

IL1R1, LIF, STAT3, STAT1, and IL1α CRISPR/Cas9 Knockout

To knock out IL1R1, STAT3, STAT1, and LIF in PSCs, lenti-Cas9-Blast plasmids (52962; Addgene) were used. PSCs were infected and selected using 2 μg/mL blasticidin (A11139-03; Thermo Fisher Scientific). Single guide RNAs (sgRNA) were designed using CRISPR Design (http://crispr.mit.edu) and cloned into the LRGN (Lenti-sgRNA-EFS-GFP-neo) plasmid. Cleavage was confirmed using the GeneArt Genomic Cleavage Detection Kit (A24372; Invitrogen). PSCs were plated as single clones in 96-well plates in the presence of neomycin (10131035; Invitrogen). Generation of IL6 KO PSCs was previously described (19). To knock out IL1α in tumor organoids, LentiV_Cas9_puro plasmids were used. Tumor organoids were infected and selected using 2.5 μg/mL puromycin (A1113803; Thermo Scientific). sgRNAs were designed, cloned, and validated as above. Organoids were infected and plated as single cells in the presence of neomycin. Knockout was confirmed by Sanger sequencing and western blot analysis or ELISA. gRNA-resistant IL1R1 cDNA was generated by site-directed mutagenesis of the gRNA PAM sequence using the QuikChange Lightning Site-Directed Mutagenesis kit (210515; Agilent). Wild-type mouse IL1R1 cDNA (MC219163; Origene) was PCR amplified with mutagenic primers to induce a G>T transversion, thereby converting codon 8 from GGG>GGT.

qPCR Analysis

RNA (1 μg) was reverse transcribed using TaqMan reverse transcription reagents (N808-0234; Applied Biosystems). qPCR was performed using gene-specific TaqMan probes (Applied Biosystems) and master mix (4440040; Applied Biosystems). Gene expression was normalized to *Hprt*.

Nuclear Fractionation

PSCs were harvested in Cell Recovery Solution (354253; Corning) and incubated rotating for 30 minutes at 4°C. Pellets were lysed with 10 mmol/L Tris pH 8.0, 10 mmol/L NaCl, and 0.2% NP-40, incubated on ice for 15 minutes and spun down. Supernatants containing cytoplasmic fractions were collected. Pellets were resuspended in 50 mmol/L Tris pH 8.0, 10 mmol/L EDTA, and 1% SDS, incubated on ice for 10 minutes, sonicated and spun down at maximum speed for 15 minutes. Supernatants containing nuclear fractions were collected.

Western Blot Analysis

PSCs and organoids were harvested in Cell Recovery Solution and incubated rotating for 30 minutes at 4°C. Cells were pelleted and lysed in 0.1% Triton X-100, 15 mmol/L NaCl, 0.5 mmol/L EDTA, 5 mmol/L Tris, pH 7.5, supplemented with complete, mini protease inhibitors (11836170001; Roche) and a phosphatase inhibitor cocktail (4906845001; Roche). Cells were incubated on ice for 30 minutes before clarification. Standard procedures were used for western blotting. Primary antibodies used were αSMA (M0851; Dako), HSP90α (07-2174; EMD Millipore), ACTIN (8456; Cell Signaling Technology), STAT3 (9139; Cell Signaling Technology), pSTAT3 (9145; Cell Signaling Technology), STAT1 (9172; Cell Signaling Technology), pSTAT1 (9167; Cell Signaling Technology), IL1R1 (AF771; R&D Systems), pJAK1 (3331; Cell Signaling Technology), JAK1 (MAB42601-SP; R&D Systems), pJAK2 (3771; Cell Signaling Technology), JAK2 (3230; Cell Signaling Technology), p-p65 (3033; Cell Signaling Technology), p65 (8242; Cell Signaling Technology), H3 (ab4729; Abcam), SMAD4 (sc-7966; Santa Cruz), SMAD2 (5339; Cell Signaling Technology), pSMAD2 (8828; Cell Signaling Technology), SMAD3 (9513; Cell Signaling Technology), pSMAD3 (9530; Cell Signaling Technology), CTGF (ab125943; Abcam), IκBα (4814; Cell Signaling Technology), pIκBα (9246; Cell Signaling Technology). Proteins were detected using HRP-conjugated secondary antibodies (Jackson ImmunoResearch Laboratories).

ELISA and Luminex Assays

For ELISA of media, cultures were grown for 3 to 5 days. Media were collected, spun down, and assayed using the manufacturer's protocol. ELISA assays used were TNFα (MTA00B; R&D Systems) and IL1α (MLA00; R&D Systems). A Milliplex Mouse Cytokine/Chemokine Magnetic Bead Premixed 32 Plex Kit (MCYTMAG-70K-PX32; EMD Millipore) was run on a MAGPIX (MAGPIX-XPONENT, Luminex) to detect G-CSF, IL6, and LIF.

Proliferation Assays

For proliferation assays of PSCs in Matrigel, 6,000 PSCs were plated in 52 μL of 50% Matrigel in PBS on white 96-well plates (136101; Corning) and cultured in 100 μL of media. For proliferation assays in monolayer, 500 PSCs were plated on white 96-well plates and cultured in 100 μL of DMEM with 5% FBS. For proliferation assays of organoids, 700 single cells were plated on white 96-well plates in 200 μL of 10% Matrigel in DMEM with 5% FBS. Proliferation was followed for 5 to 6 days with CellTiter-Glo (G7573; Promega), with measurements every 24 hours.

Immunofluorescence and IHC Staining of Tissues

Human PDAC tissues were purchased from US Biomax, which collects all human tissues under HIPAA-approved protocols (HPanAde060CS-01; US Biomax). Standard procedures were used for IHC and immunofluorescence (IF) staining. Primary antibodies for IF were pSTAT3, pSMAD2 (3108; Cell Signaling Technology), αSMA (M0851; Dako), and E-cadherin (610181; BD Biosciences). Secondary antibodies were anti-mouse Alexa Fluor 568 (A10037; Thermo

Fisher Scientific) and HRP anti-rabbit (PI1000; Vector Laboratories). The PerkinElmer TSA Fluorescein System was used to detect pSTAT3 or pSMAD2 (NEL701A001KT for mouse and human pSMAD2 and mouse pSTAT3, and NEL744001KT for human pSTAT3). DAPI (D8417; Sigma-Aldrich) was used as counterstain. Sections were mounted with Prolong Gold antifade reagent (P10144; Invitrogen). Primary antibodies for IHC were pSTAT3, pSMAD2, E-cadherin, αSMA (ab5694; Abcam), pH3 (9701; Cell Signaling Technology). For sequential IHC, DAB (SK-4105; Vector Laboratories), and VIP (SK-4605; Vector Laboratories) were used for different primary antibodies. Hematoxylin was used as nuclear counterstain. Hematoxylin and eosin and Masson's trichrome stainings were performed according to standard protocols. Fluorescence imaging of tissue was done with a Leica TCS SP8 laser scanning confocal (Boulder Grove Il), controlled by the LAS AF 3.3.10134 software. Immunofluorescence images were quantified using the population analysis module in Volocity (Improvision). Brightfield images of tissue slides were obtained with an Axio Imager.A2 (ZEISS). Stained sections were scanned with Aperio ScanScope CS and analyzed using the ImageScope Positive Pixel Count algorithm. To quantify Masson's trichrome stain, hue values for blue and pink were measured using an average hue value of 0.6 and a hue width of 0.854. The percentage of the collagen area was then determined by calculating the percentage of blue pixels relative to the entire stained area. To quantify αSMA stain, the percentage of strong positive pixels was calculated relative to the entire section with the ImageScope software. To quantify pSTAT3, pSMAD2, and pH3, the percentage of strong positive nuclei was calculated relative to the total number of nuclei with the ImageScope nuclear v9 algorithm.

In Vivo *Orthotopic Transplantations*

Orthotopic injections were conducted as previously described (17). Cells (2.5×10^5) prepared from organoid cultures were resuspended as a 45 μL suspension of 50% Matrigel in PBS and injected into the pancreas. Rosa26-targeted and IL1α knockout tumors were imaged using the Vevo 3100 Ultrasound at two different orientations with respect to the transducer. Tumor volumes were measured at two angles using the Vevo LAB software program (version 2.2.0).

AZD1480 and LY2157299 Treatment in KPC Mice

KPC mice were subjected to high-contrast ultrasound imaging using a Vevo 3100 Ultrasound with an MS250X transducer (Fujifilm VisualSonics). Mice with tumor diameters of 6 to 7 mm were randomized and enrolled 1 day after scanning. The JAK inhibitor AZD1480 was prepared daily as a suspension in 0.1% Tween80, 0.5% hydroxyl propyl methyl cellulose in sterile water. Mice were administered vehicle or 50 mg/kg of AZD1480 for 10 days, once a day via oral gavage. The TGFBR inhibitor galunisertib (LY2157299) was prepared daily as a suspension in 0.5% hydroxyl propyl methyl cellulose in sterile water. Mice were administered vehicle or 75 mg/kg of LY2157299 for 10 days, twice a day via oral gavage. Tumors were imaged using the Vevo 3100 Ultrasound at two different orientations with respect to the transducer. Tumor volumes were measured at two angles, if possible, using the Vevo LAB software program (version 2.2.0).

Flow Cytometry and Cell Sorting

For sorting of cancer cells and CAFs, KPC tumors were processed as previously described (19). Cells were stained for 30 minutes with anti-mouse CD45-AlexaFluor 647 (103124; BioLegend), CD326 (EPCAM)-AlexaFluor 488 (118212; BioLegend), CD31-AlexaFluor 647 (102416; BioLegend), CD140a (PDGFRα)-PE (135905; BioLegend), PDPN-APC/Cy7 (127418; BioLegend), and DAPI for 15 minutes. Cells were sorted on the FACSAria cell sorter (BD) for DAPI/CD45/CD31$^-$ EPCAM$^+$ and DAPI/CD45/CD31/EpCAM$^-$ PDPN$^+$ cell populations. For flow cytometry analysis of EdU-treated KPC tumors, KPC mice were administered 300 μg EdU (61135-33-9; Santa Cruz) formulated in sterile saline twice a day for 3 days via intraperitoneal injection. EdU was detected using the Click-iT Plus EdU Alexa Fluor 647 Flow Cytometry Assay Kit (C10634; Thermo Fisher Scientific). For flow-cytometric analysis of IL1R1 and myCAF/iCAF populations, antibodies used were anti-mouse CD31-PE/Cy7 (102418; BioLegend), CD45-PerCP/Cy5.5 (103132; BioLegend), CD326 (EPCAM)-AlexaFluor 488, PDPN-APC/Cy7, CD140a (PDGFRα)-PE, Ly6C-APC (128015; BioLegend), biotinylated CD121a (IL1R, Type I/p80; 113503; BioLegend), and APC streptavidin (405207; BioLegend).

RNA-Sequencing Library Construction and Analysis

Samples were collected in 1 mL of TRIzol Reagent (15596-018; Thermo Fisher Scientific). RNA was extracted using the PureLink RNA mini kit (12183018A; Thermo Fisher Scientific). RNA quality was assessed on a bioanalyzer using the Agilent RNA 6000 Nano kit (5067-1511; Agilent). We used the TruSeq Stranded Total RNA Kit with RiboZero Human/Mouse/Rat (RS-122-2202; Illumina; 0.2–1 μg per sample, RNA integrity number > 8) and proceeded to library preparation using an Illumina TruSeq RNA prep kit (IP-202-1012 and IP-202-1024; Illumina). Libraries were then sequenced using Illumina NextSeq500. All RNA-sequencing data are available at the Gene Expression Omnibus (GEO) under the accession number GSE113615. Protein coding genes expressed in at least two samples were included for differential expression analysis (DEA). DEA was performed using DESeq program (V2) with default parameters. Genes with adjusted $P < 0.05$ were selected as significantly changed between conditions. The principal components for variance-stabilized data were estimated using plotPCA function available in DESeq and plotted using the ggplot2 function in R. GSEA was performed using the GSEA program (Broad Institute) on the C2 canonical pathway collection (C2.cp.v5.1) downloaded from the Molecular Signatures Database (MSigDB). Genes were ranked by their *P* values before submitted to GSEA for analysis.

STAT3 and SMAD2/3/4 Motif Searching

STAT3 and SMAD2/3/4 human and mouse motif position weight matrices were downloaded from the JASPAR 2018 database. Promoter sequences (−5 kbp/200 bp surrounding transcription start sites) were prepared by custom R and Shell scripts for both hg19 and mm10 genomes. Motif searching was performed using FIMO program available in MEME Suite with $P < 1e4$ as hit cutoff.

Single-Cell RNA Sequencing of KPC Tumors

Tumors were digested as previously described (19). Single-cell barcoded cDNA libraries were generated using the 10× Genomics Chromium Controller via the Single-Cell 3′ Library Kit (120237; 10× Genomics). Libraries were sequenced on a NextSeq500 (Illumina). Library batches were normalized using the CellRanger Aggregate function, and the resulting gene-barcode matrices were fed into SCANPY (53). Dimensionality reduction was carried out in SCANPY via principal component analysis followed by Louvain clustering t-SNE visualization using the top 20 significant components. Major clusters were denoted by differentially expressed canonical marker genes, and these were subjected to additional rounds of cluster refinement. All single-cell RNA-sequencing data are available at GEO under the accession number GSE114417. DEA was performed using the SCDE program (54). Differentially expressed genes (adjusted $P < 0.05$) were ranked by Z scores reported by SCDE and submitted to the GSEA program (55). DE genes were compared with their counterparts from a bulk RNA-sequencing data set (19). Overlap *P* values were calculated using the *phyper* function in R. Venny program was used to produce the Venn diagrams. To generate heat maps, the preprocessed data matrices were passed from SCANPY to the Seurat package (PMCID: PMC4430369),

and marker genes discriminating the fibroblast subpopulations were identified using the FindMarkers function. The top 25 markers ranked by Bonferroni adjusted *P* values are displayed on a log (10) fold-change color scale, normalized across all cells.

Statistical Analysis

GraphPad Prism was used for graphical representation of data. Statistical analysis was performed using Student *t* test.

Disclosure of Potential Conflicts of Interest

D.A. Tuveson reports receiving commercial research grants from ONO and Fibrogen, has ownership interest (including stock, patents, etc.) in Leap Therapeutics and Surface Oncology, and is a consultant/advisory board member for Leap Therapeutics, Surface Oncology, MabImmune, and Bethyl Antibodies. No potential conflicts of interest were disclosed by the other authors.

Authors' Contributions

Conception and design: G. Biffi, D.A. Tuveson
Development of methodology: J. Preall
Acquisition of data (provided animals, acquired and managed patients, provided facilities, etc.): G. Biffi, T.E. Oni, B. Spielman
Analysis and interpretation of data (e.g., statistical analysis, biostatistics, computational analysis): G. Biffi, Y. Hao, J. Preall
Writing, review, and/or revision of the manuscript: G. Biffi, T.E. Oni, E. Elyada, Y. Park, D.A. Tuveson
Study supervision: D.A. Tuveson
Other (overviewed the *in vivo* animal work): Y. Park

Acknowledgments

The authors would like to thank the Cold Spring Harbor Cancer Center Support Grant (CCSG) shared resources: Bioinformatics Shared Resource, Next Generation Sequencing Core Facility, P. Moody and C. Kanzler in the Flow Cytometry Facility, Animal and Tissue Imaging, and the Animal Facility. The CCSG is funded by the NIH Cancer Center Support Grant 5P30CA045508. We thank Dr. L. Baker for critical review of the manuscript. We thank Dr. J. Ipsaro for the initial biochemical characterization of tumor organoid–conditioned media. We thank Dr. F. Greten for kindly providing us with ML102B. This work was supported by the Lustgarten Foundation, where D.A. Tuveson is a distinguished scholar and Director of the Lustgarten Foundation–designated Laboratory of Pancreatic Cancer Research. D.A. Tuveson is also supported by the Cold Spring Harbor Laboratory Association and the National Institutes of Health (NIH 5P30CA45508, 5P50CA101955, P20CA192996, U10CA180944, U01CA210240, U01CA224013, 1R01CA188134, and 1R01CA190092). In addition, we are grateful for support from the following: the Human Frontiers Science Program (LT000195/2015-L for G. Biffi and LT000403/2014-L for E. Elyada), EMBO (ALTF 1203-2014 for G. Biffi), The Cold Spring Harbor Laboratory and Northwell Health Affiliation (for J. Preall and D.A. Tuveson), and the NIH (R50 CA211506 for Y. Park).

Received June 26, 2018; revised September 20, 2018; accepted October 19, 2018; published first October 26, 2018.

REFERENCES

1. Siegel RL, Miller KD, Jemal A. Cancer statistics, 2016. CA Cancer J Clin 2016;66:7–30.
2. Jacobetz MA, Chan DS, Neesse A, Bapiro TE, Cook N, Frese KK, et al. Hyaluronan impairs vascular function and drug delivery in a mouse model of pancreatic cancer. Gut 2013;62:112–20.
3. Olive KP, Jacobetz MA, Davidson CJ, Gopinathan A, McIntyre D, Honess D, et al. Inhibition of Hedgehog signaling enhances delivery of chemotherapy in a mouse model of pancreatic cancer. Science 2009;324:1457–61.
4. Provenzano PP, Cuevas C, Chang AE, Goel VK, Von Hoff DD, Hingorani SR. Enzymatic targeting of the stroma ablates physical barriers to treatment of pancreatic ductal adenocarcinoma. Cancer Cell 2012;21:418–29.
5. Diop-Frimpong B, Chauhan VP, Krane S, Boucher Y, Jain RK. Losartan inhibits collagen I synthesis and improves the distribution and efficacy of nanotherapeutics in tumors. Proc Natl Acad Sci U S A 2011;108:2909–14.
6. Hwang RF, Moore T, Arumugam T, Ramachandran V, Amos KD, Rivera A, et al. Cancer-associated stromal fibroblasts promote pancreatic tumor progression. Cancer Res 2008;68:918–26.
7. Long KB, Tooker G, Tooker E, Luque SL, Lee JW, Pan X, et al. IL6 Receptor blockade enhances chemotherapy efficacy in pancreatic ductal adenocarcinoma. Mol Cancer Ther 2017;16:1898–908.
8. Singh S, Srivastava SK, Bhardwaj A, Owen LB, Singh AP. CXCL12-CXCR4 signalling axis confers gemcitabine resistance to pancreatic cancer cells: a novel target for therapy. Br J Cancer 2010;103:1671–9.
9. Straussman R, Morikawa T, Shee K, Barzily-Rokni M, Qian ZR, Du J, et al. Tumour micro-environment elicits innate resistance to RAF inhibitors through HGF secretion. Nature 2012;487:500–4.
10. Hessmann E, Patzak MS, Klein L, Chen N, Kari V, Ramu I, et al. Fibroblast drug scavenging increases intratumoural gemcitabine accumulation in murine pancreas cancer. Gut 2018;67:497–507.
11. Feig C, Jones JO, Kraman M, Wells RJ, Deonarine A, Chan DS, et al. Targeting CXCL12 from FAP-expressing carcinoma-associated fibroblasts synergizes with anti-PD-L1 immunotherapy in pancreatic cancer. Proc Natl Acad Sci U S A 2013;110:20212–7.
12. Sherman MH, Yu RT, Engle DD, Ding N, Atkins AR, Tiriac H, et al. Vitamin D receptor-mediated stromal reprogramming suppresses pancreatitis and enhances pancreatic cancer therapy. Cell 2014;159:80–93.
13. Lee JJ, Perera RM, Wang H, Wu DC, Liu XS, Han S, et al. Stromal response to Hedgehog signaling restrains pancreatic cancer progression. Proc Natl Acad Sci U S A 2014;111:E3091–100.
14. Rhim AD, Oberstein PE, Thomas DH, Mirek ET, Palermo CF, Sastra SA, et al. Stromal elements act to restrain, rather than support, pancreatic ductal adenocarcinoma. Cancer Cell 2014;25:735–47.
15. Kim EJ, Sahai V, Abel EV, Griffith KA, Greenson JK, Takebe N, et al. Pilot clinical trial of hedgehog pathway inhibitor GDC-0449 (vismodegib) in combination with gemcitabine in patients with metastatic pancreatic adenocarcinoma. Clin Cancer Res 2014;20:5937–45.
16. Ozdemir BC, Pentcheva-Hoang T, Carstens JL, Zheng X, Wu CC, Simpson TR, et al. Depletion of carcinoma-associated fibroblasts and fibrosis induces immunosuppression and accelerates pancreas cancer with reduced survival. Cancer Cell 2014;25:719–34.
17. Boj SF, Hwang CI, Baker LA, Chio II, Engle DD, Corbo V, et al. Organoid models of human and mouse ductal pancreatic cancer. Cell 2015;160:324–38.
18. Hingorani SR, Wang L, Multani AS, Combs C, Deramaudt TB, Hruban RH, et al. Trp53R172H and KrasG12D cooperate to promote chromosomal instability and widely metastatic pancreatic ductal adenocarcinoma in mice. Cancer Cell 2005;7:469–83.
19. Ohlund D, Handly-Santana A, Biffi G, Elyada E, Almeida AS, Ponz-Sarvise M, et al. Distinct populations of inflammatory fibroblasts and myofibroblasts in pancreatic cancer. J Exp Med 2017;214:579–96.
20. Bernard V, Semaan A, Huang J, San Lucas FA, Mulu FC, Stephens BM, et al. Single cell transcriptomics of pancreatic cancer precursors demonstrates epithelial and microenvironmental heterogeneity as an early event in neoplastic progression. Clin Can Res 2018 Nov 1 [Epub ahead of print].
21. Albrengues J, Bertero T, Grasset E, Bonan S, Maiel M, Bourget I, et al. Epigenetic switch drives the conversion of fibroblasts into proinvasive cancer-associated fibroblasts. Nat Commun 2015;6:10204.
22. Corcoran RB, Contino G, Deshpande V, Tzatsos A, Conrad C, Benes CH, et al. STAT3 plays a critical role in KRAS-induced pancreatic tumorigenesis. Cancer Res 2011;71:5020–9.
23. Lesina M, Kurkowski MU, Ludes K, Rose-John S, Treiber M, Kloppel G, et al. Stat3/Socs3 activation by IL-6 transsignaling promotes

progression of pancreatic intraepithelial neoplasia and development of pancreatic cancer. Cancer Cell 2011;19:456–69.
24. Li J, Byrne KT, Yan F, Yamazoe T, Chen Z, Baslan T, et al. Tumor cell-intrinsic factors underlie heterogeneity of immune cell infiltration and response to immunotherapy. Immunity 2018;49:178–93 e7.
25. Erez N, Truitt M, Olson P, Arron ST, Hanahan D. Cancer-Associated Fibroblasts are activated in incipient neoplasia to orchestrate tumor-promoting inflammation in an NF-kappaB-dependent manner. Cancer Cell 2010;17:135–47.
26. Su S, Chen J, Yao H, Liu J, Yu S, Lao L, et al. CD10(+)GPR77(+) cancer-associated fibroblasts promote cancer formation and chemoresistance by sustaining cancer stemness. Cell 2018;172:841–56 e16.
27. Egberts JH, Cloosters V, Noack A, Schniewind B, Thon L, Klose S, et al. Anti-tumor necrosis factor therapy inhibits pancreatic tumor growth and metastasis. Cancer Res 2008;68:1443–50.
28. Ling J, Kang Y, Zhao R, Xia Q, Lee DF, Chang Z, et al. KrasG12D-induced IKK2/beta/NF-kappaB activation by IL-1alpha and p62 feedforward loops is required for development of pancreatic ductal adenocarcinoma. Cancer Cell 2012;21:105–20.
29. Melisi D, Niu J, Chang Z, Xia Q, Peng B, Ishiyama S, et al. Secreted interleukin-1alpha induces a metastatic phenotype in pancreatic cancer by sustaining a constitutive activation of nuclear factor-kappaB. Mol Cancer Res 2009;7:624–33.
30. Niu J, Li Z, Peng B, Chiao PJ. Identification of an autoregulatory feedback pathway involving interleukin-1alpha in induction of constitutive NF-kappaB activation in pancreatic cancer cells. J Biol Chem 2004;279:16452–62.
31. Zhuang Z, Ju HQ, Aguilar M, Gocho T, Li H, Iida T, et al. IL1 receptor antagonist inhibits pancreatic cancer growth by abrogating NF-kappaB activation. Clin Cancer Res 2016;22:1432–44.
32. Tjomsland V, Spangeus A, Valila J, Sandstrom P, Borch K, Druid H, et al. Interleukin 1alpha sustains the expression of inflammatory factors in human pancreatic cancer microenvironment by targeting cancer-associated fibroblasts. Neoplasia 2011;13:664–75.
33. Zhang D, Li L, Jiang H, Li Q, Wang-Gillam A, Yu J, et al. Tumor-stroma IL1beta-IRAK4 feedforward circuitry drives tumor fibrosis, chemoresistance, and poor prognosis in pancreatic cancer. Cancer Res 2018;78:1700–12.
34. Zhao X, Fan W, Xu Z, Chen H, He Y, Yang G, et al. Inhibiting tumor necrosis factor-alpha diminishes desmoplasia and inflammation to overcome chemoresistance in pancreatic ductal adenocarcinoma. Oncotarget 2016;7:81110–22.
35. Wen D, Nong Y, Morgan JG, Gangurde P, Bielecki A, Dasilva J, et al. A selective small molecule IkappaB Kinase beta inhibitor blocks nuclear factor kappaB-mediated inflammatory responses in human fibroblast-like synoviocytes, chondrocytes, and mast cells. J Pharmacol Exp Ther 2006;317:989–1001.
36. Glaccum MB, Stocking KL, Charrier K, Smith JL, Willis CR, Maliszewski C, et al. Phenotypic and functional characterization of mice that lack the type I receptor for IL-1. J Immunol 1997;159:3364–71.
37. Phan VT, Wu X, Cheng JH, Sheng RX, Chung AS, Zhuang G, et al. Oncogenic RAS pathway activation promotes resistance to anti-VEGF therapy through G-CSF-induced neutrophil recruitment. Proc Natl Acad Sci U S A 2013;110:6079–84.
38. Pickup MW, Owens P, Gorska AE, Chytil A, Ye F, Shi C, et al. Development of aggressive pancreatic ductal adenocarcinomas depends on granulocyte colony stimulating factor secretion in carcinoma cells. Cancer Immunol Res 2017;5:718–29.
39. Hedvat M, Huszar D, Herrmann A, Gozgit JM, Schroeder A, Sheehy A, et al. The JAK2 inhibitor AZD1480 potently blocks Stat3 signaling and oncogenesis in solid tumors. Cancer Cell 2009;16:487–97.
40. Fleming JD, Giresi PG, Lindahl-Allen M, Krall EB, Lieb JD, Struhl K. STAT3 acts through pre-existing nucleosome-depleted regions bound by FOS during an epigenetic switch linking inflammation to cancer. Epigenetics Chromatin 2015;8:7.
41. Evans RA, Tian YC, Steadman R, Phillips AO. TGF-beta1-mediated fibroblast-myofibroblast terminal differentiation-the role of Smad proteins. Exp Cell Res 2003;282:90–100.
42. Vaughan MB, Howard EW, Tomasek JJ. Transforming growth factor-beta1 promotes the morphological and functional differentiation of the myofibroblast. Exp Cell Res 2000;257:180–9.
43. Ding N, Yu RT, Subramaniam N, Sherman MH, Wilson C, Rao R, et al. A vitamin D receptor/SMAD genomic circuit gates hepatic fibrotic response. Cell 2013;153:601–13.
44. Yingling JM, McMillen WT, Yan L, Huang H, Sawyer JS, Graff J, et al. Preclinical assessment of galunisertib (LY2157299 monohydrate), a first-in-class transforming growth factor-beta receptor type I inhibitor. Oncotarget 2018;9:6659–77.
45. Flint TR, Janowitz T, Connell CM, Roberts EW, Denton AE, Coll AP, et al. Tumor-induced IL-6 reprograms host metabolism to suppress anti-tumor immunity. Cell Metab 2016;24:672–84.
46. Mace TA, Shakya R, Pitarresi JR, Swanson B, McQuinn CW, Loftus S, et al. IL-6 and PD-L1 antibody blockade combination therapy reduces tumour progression in murine models of pancreatic cancer. Gut 2018;67:320–32.
47. Hurwitz H, Van Cutsem E, Bendell J, Hidalgo M, Li CP, Salvo MG, et al. Ruxolitinib + capecitabine in advanced/metastatic pancreatic cancer after disease progression/intolerance to first-line therapy: JANUS 1 and 2 randomized phase III studies. Invest New Drugs 2018.
48. Hurwitz HI, Uppal N, Wagner SA, Bendell JC, Beck JT, Wade SM 3rd, et al. Randomized, double-blind, phase II study of ruxolitinib or placebo in combination with capecitabine in patients with metastatic pancreatic cancer for whom therapy with gemcitabine has failed. J Clin Oncol 2015;33:4039–47.
49. Nagathihalli NS, Castellanos JA, Shi C, Beesetty Y, Reyzer ML, Caprioli R, et al. Signal transducer and activator of transcription 3, mediated remodeling of the tumor microenvironment results in enhanced tumor drug delivery in a mouse model of pancreatic cancer. Gastroenterology 2015;149:1932–43 e9.
50. Wörmann SM, Song L, Ai J, Diakopoulos KN, Görgülü K, Ruess D, et al. Loss of P53 function activates JAK2–STAT3 signaling to promote pancreatic tumor growth, stroma modification, and gemcitabine resistance in mice and is associated with patient survival. Gastroenterology 2016;151:180–93.e12.
51. Laklai H, Miroshnikova YA, Pickup MW, Collisson EA, Kim GE, Barrett AS, et al. Genotype tunes pancreatic ductal adenocarcinoma tissue tension to induce matricellular fibrosis and tumor progression. Nat Med 2016;22:497–505.
52. Zhao S, Venkatasubbarao K, Lazor JW, Sperry J, Jin C, Cao L, et al. Inhibition of STAT3 Tyr705 phosphorylation by Smad4 suppresses transforming growth factor beta-mediated invasion and metastasis in pancreatic cancer cells. Cancer Res 2008;68:4221–8.
53. Wolf FA, Angerer P, Theis FJ. SCANPY: large-scale single-cell gene expression data analysis. Genome Biol 2018;19:15.
54. Kharchenko PV, Silberstein L, Scadden DT. Bayesian approach to single-cell differential expression analysis. Nat Methods 2014;11:740–2.
55. Subramanian A, Tamayo P, Mootha VK, Mukherjee S, Ebert BL, Gillette MA, et al. Gene set enrichment analysis: a knowledge-based approach for interpreting genome-wide expression profiles. Proc Natl Acad Sci U S A 2005;102:15545–50.